國 立 交 通 大 學

電子工程學系 電子研究所

碩 士 論 文

磁性 FePt 奈米點 MIS 電容的異值崩潰電壓的特性與分析

The Characteristics of Anomalous Breakdown Strength in Magnetic FePt Nanodots MIS Capacitor

研 究 生：江培維

指導教授：張俊彥 院士

中 華 民 國 九 十 九 年 七 月

磁性 FePt 奈米點 MIS 電容的異值崩潰電壓的特性與分析

The Characteristics of Anomalous Breakdown Strength in Magnetic FePt Nanodots MIS Capacitor

研 究 生：江培維　　Student：Pei-Wei Chiang

指導教授：張俊彥 院士　　Advisor：Prof. Chun-Yen Chang

國 立 交 通 大 學

電子工程學系 電子研究所

碩 士 論 文

A Thesis

Submitted to Department of Electronics Engineering & Institute of Electronics

College of Electrical and Computer Engineering

National Chiao Tung University

In Partial Fulfillment of the Requirements

For the Degree of

Master

In

Electronics Engineering

July 2010

Hsinchu, Taiwan, Republic of China

中華民國九十九年七月

磁性 FePt 奈米點 MIS 電容的異值崩潰電壓的特性與分析

學生：江培維　　　　　　　　　　　　指導教授：張俊彥 院士

國立交通大學電子工程學系電子研究所碩士班

摘要

在半導體的領域中，研究的主流往往是矽半導體、高介電材料、三五族復合物。多數被視為前段製程汙染物的磁性材料在半導體界上的應用則顯得特別的少，然而，我們發現磁性物質應用在金-氧-半電容中卻有增強電場電度的特殊現象。而本論文就以此現象進行分析與討論，用量子力學的觀點來解釋並以模擬軟體加以佐證。

本論文討論分為兩大部分，第一部分為磁性薄膜 FePt 的製備為分析，其中我們也探討了磁性與熱退火的關係，另一部分則在電容中埋入磁性奈米點，並探討其在極薄氧化層(34nm)中異常高的崩潰電壓(49.2V)，並以量子力學及 COMSOL 複合物理模擬軟體去解釋在磁場下電子的波函數發生的 localize 效應。藉由討論磁性奈米點金氧半電容的漏電現象來間接應證磁性物質在介電層中的載子傳輸機制的影響。

The Characteristics of Anomalous Breakdown Strength in Magnetic FePt Nanodots MIS Capacitor

Student: Pei-Wei Chiang Advisor: Prof. Chun-Yen Chang

Department of Electronics Engineering and Institute of Electronics
National Chiao Tung University

Abstract

In the field of semiconductor, the main stream research is always on standard process, such as Si-based semiconductor, high- κ material, III-V compound semiconductor. However, the research of magnetic material applied in semiconductor is very rare. However, using magnetic effects into semiconductor, insulator, metal, superconductor related structures will open up a huge possibilities of new phenomena , new devices, new applications. In spite of that, we have found some novel characteristics in MIS capacitor with magnetic nanodot.

This thesis we have found the anomalous breakdown strength and leakage of magnetic nanodot in insulator. We presented in two parts, one is focus on FePt magnetic films fabrication, the second is that embedded FePt magnetic nanodot in oxide in MIS structure. First, FePt and oxide are deposited layer by layer. After furnace annealing, FePt dispense in oxide and induce to vertical and parallel magnetic field. This Capacitor has the anomalous huge breakdown voltage about 49V was observed in MIS capacitors with 34 nm oxide layer. We can also find huge voltage strength and we try to explain this phenomenon by quantum mechanical simulations.

On the other hand, fitting its leakage current density to find carrier transport mechanism .We also found that the wavefunction is localized under strong magnetic field in COMSOL simulation. Unfortunately, verification of leakage current reduces due to magnetic field has not been observed due to lack of comparison between second set of samples. It will be further explained in the future. The tunneling probability reduced result from magnetic field quantum confinement effect. Therefore, carriers transport with other model, which quantum respect could explain.

誌謝

二年的碩士生涯瞬息即逝，在這短短的研究所生活中，讓我學習到許多，首先，我要感謝我的指導教授張俊彥院士給予我一個好的主題，並給我許多研究觀點上的看法，讓我擁有克服困難及勇於嘗試的精神，並在思維及邏輯批判上有所成長，每一次的討論，更讓我對老師學術研究的熱忱及堅持的剛毅精神更加欽佩，老師在實驗上的大力協助及諄諄教誨，仍歷歷在目。論文中所用到的模擬部分，也要感謝李義明老師的指導及分享;同時也要感謝日本東北大學的寒川誠二教授研究群及小柳光正研究群，提供我們許多值得研究的樣品及製程經驗。

研究生涯有阻力也有助力，首要感謝的助力即時伴我度過研究所生活的磁電容組學長學弟們，緯仁、耀峰、信淵、立緯學長及新進學弟安城，都是指導我完成這篇論文的最佳伙伴，也是我最得力的助手們，同時也要感謝跟我從大學一起上研究所的凱麟及同屆的朝淦，二位在研究生活上提供我許多幫助，還有哲榮、博閔、稐寯、弘斌學長，已畢業的楊博、兆欽、誌陽、耀昇、貴宇、峻丞、勝杰學長、心卉學姊，有你們的幫忙及鼓勵，讓研究生活不再單調寂寞，也要感謝同屆外掛的同學們，簡老師的吳博、宗霖、禎晏、國永，張老師的公鍇、俊任、世陽、蘭欣、思翰及管樂團的邱高跟葉媽，同是大學同學兼室友的庭輔、辛弟、陳大奶及顯示所的紅魚，不論在奈米中心與 NDL 做實驗，感謝你們的相伴，讓我度過快樂的研究時光，最後還要特別感謝清大賴志煌老師實驗室的容蔚學長等人，讓我使用你們的機台量測及給我許多寶貴的建議，及大學材料所帶過我的建融、重守及在 NDL 的宥浦學長，有你們的協助實驗分析才得以如此順利。最後還要感謝後進的學弟妹們，林緯、祐誠、昀謹、婉儀及嗨妹，有你們在更豐富了在實驗室的生活，要感謝的實在太多，給所以曾幫助過我的人，此篇論文獻給您們。

培維

Contents

摘要 .... **I**

ABSTRACT .... **II**

誌謝 .... **IV**

CONTENTS .... **V**

TABLE CAPTION .... **VII**

FIGURE CAPTION .... **VIII**

CHAPTER 1 INTRODUCTION **1**

1.1 OVERVIEW OF METAL-INSULATOR-METAL (MIM) CAPACITOR 1

1.2 INTRODUCTION TO FEPT MAGNET NANODOT (MND) 2

1.2.1 FePt magnet nanodot fabrication *2*

1.2.2 Hysteresis loop *4*

1.3 MOTIVE 4

1.4 THE ORGANIZATION OF THIS THESIS 5

CHAPTER 2 EXPERIMENTAL DETAILS **9**

2.1 INTRODUCTION TO QUANTUM CONFINEMENT 9

2.2 WAVE FUNCTIONS AND ENERGY LEVELS IN QUANTUM DOTS 10

2.3 MAGNETIC FIELD IN QUANTUM MECHANICS 12

2.3.1 Schrödinger equation with magnetic field [20][21] *12*

2.3.2 Magnetic field induce quantum confinement *13*

2.4 COMSOL SIMULATION 14

CHAPTER 3 DEVICE STRUCTURE AND FABRICATION **21**

3.1 Magnetic nanodot capacitor Fabrication (Fig.3.1)...21

3.2 Material analysis and Electric measurement 23

CHAPTER 4 EXPERIMENT RESULTS AND DISCUSSION 28

4.1 The magnetic FePt film properties...28

4.2 Properties of magnetic nanodot MIS leakage characteristics 29

4.2.1 Ohmic Conduction Fitting..29

4.2.2 Schottky Emission Fitting...30

4.2.3 Frenkel-Poole Emission Fitting 31

4.2.4 Space Charge Limited Current Fitting...32

4.2.5 Tunneling Fitting...33

4.3 The Voltage and Temperature Effect of FePt MND Capacitors 34

4.3.1 Voltage Stress on FePt MND Capacitor...35

4.3.2 Thermal Stress on FePt MND Capacitor 36

CHAPTER 5 CONCLUSION AND FUTURE WORK 55

5.1 Conclusion 55

5.2 Future Work 56

Reference 57

Table caption

TABLE 1.1. COMPARISON OF RELEVANT PROPERTIES FOR SOME HIGH-K CANDIDATES............. 6

TABLE 4.2 DIFFERENT ELEMENT CONCENTRATION RATIO OF FE:PT MEASURED BY ICP-MS .. 42

TABLE 4.2 MAGNETIZATION VALUE OF FEPT MND MAGNETIC HYSTERESIS 43

TABLE 4.3 CNDUCTION MECHANISMS[30].. 44

Figure caption

Figure 1.1 Different MIM structure (a) sandwich MIM[5] (b)laminate MIM structure[6]……………7

Figure 1.2 TEM micrograph of a assembly of 6-nm as-synthesized $Fe_{50}Pt_{50}$ particles deposited from a hexane/octane dispersion on SiO-coated copper grid nanodot (B) Replacing oleic acid/oleyl amine with hexanoic acid/hexy-lamine. (C) HRSEM image after annealed at 560℃ for 30min under N_2 gas. (D) High resolution TEM image of $Fe_{52}Pt_{48}$ annealed at 560℃ for 30min.[14]……………………………………………………………………………..7

Figure 1.3 Schematic figure of SAND method………………………………………………………8

Figure 1.4 Hysteresis loop……………………………………………………………………………8

Figure 2.1 Sketch of a quantum box embedded in a matrix…………………………………………16

Figure 2.2 Schematic presentation of the wavefunction altered with magnetic field in quantum wells (a) under magnetic field (b)under electric field and magnetic field……………………………16

Figure 2.3 Five quantum wells with width 2nm, spacing 2nm, depth 1.0eV with ky=0……………….17

Figure 2.4 Probability in center well with different spacing in well width 2nm, well depth 1.0eV……17

Figure 2.5 Probability in center well with different well width in well spacing 2nm, well depth 1.0eV……………………………………………………………………………………..18

Figure 2.6 Probability in center well with different effective mass in well spacing 2nm,well width 2nm, well depth 5.0eV…………………………………………………………………………18

Figure2.7 The magnetic field can suppress the tunneling probability more effectively with small electron mass……………………………………………………………………………..19

Figure 2.8 The magnetic field can suppress the tunneling probability more effectively with large bias voltage…………………………………………………………………………………19

Figure 2.9 The magnetic field can suppress the tunneling probability more effectively with lower

barrier height……………………………………………………………………………..20

Figure 2.10 The magnetic field can suppress the tunneling probability more effectively with wider barrier width…………………………………………………………………………...20

Figure 3.1 The process flow(a)stpe1 (b)step2 (c)step3 (d)step4 (e)step6………………………………25

Figure 3.2 Vibrating Sample Magnetometer (VSM) structure………………………………………….26

Figure 3.3 Transmission electron microscope(TEM) morphology of cross section (a)cross structure (b)scale 20nm(c)scale 5nm……………………………………………………………………27

Figure 4.1 *XRD* pattern of *FePt* thin film with different annealing temperature for 30min (a)400℃ (b)500℃ (c)600℃ ……………………………………………………………………..37

Figure 4.2 Magnetic hysteresis loop of *FePt* thin film parallel magnetic field with different element ratio…………………………………………………………………………………………38

Figure 4.3 Magnetic hysteresis loop of *FePt* thin film fabricate on different underlayer……………..38

Figure 4.4 Magnetic hysteresis loop of *MND MIS* capacitor after magnetic annealing 700℃ 60 min.…………………………………………………………………………………………40

Figure 4.5 *J-V* ofmagnetic *FePt* nanodot *MIS* capacitor with different Al top electrode area…………41

Figure 4.6 Ohmic Conduction Fitting (a)accumulation mode (b)depletion mode……………………..42

Figure 4.7 Schottky emission fitting (a)*J-V* (b) the Schottky relationship of $ln(J/T^2)$ verse *1/kT*...........43

Figure 4.8 Extract slop from Fig.4.7(b)…………………………………………………………...44

Figure 4.9 Frenkel-Poole emission fitting (a)*J-V* (b) Frenkel-Poole thermal relationship……………..45

Figure 4.10 Extract slop from Fig.4.9(b)…………………………………………………………….46

Figure 4.11 *J-V* characteristic of *MIS* capacitor compares with *FePt MND* and non-*MND*……………46

Figure 4.12 *SCLC* fitting (a)accumulation mode (b)depletion mode…………………………………...47

Figure 4.13 Tunneling fitting (a)accumulation mode (b)depletion mode ………………………………48

Figure 4.14 Leakage current mechanism fitting (a) accumulation mode (b) depletion mode………….49

Figure 4.15 Current density with 20V constant voltage stress during 10000 second…………………..50

Figure 4.16 *J-V* with constant voltage stress (a)accumulation mode (b)depletion mode………………51

Figure 4.17 *C-V* with constant voltage stress 20V during 10000s……………………………………..52

Figure 4.18 FePt MND capacitor *C-V* characteristic with thermal stress at (a)1MHz (b)1kHZ……….53

Figure 4.19 FePt MND capatior *J-V* characteristic with thermal stress………………………………...54

Chapter 1

Introduction

1.1 Overview of Metal-insulator-Metal (MIM) capacitor

The metal-insulator-metal (MIM) capacitor is one of the most important passive device in radio-frequency and analog signal IC applications. The dramatic increase in wired and wireless communications has triggered the demand on MIM capacitors with low parasitic, high quality factor, and low voltage coefficients [1].

In the conventional metal-insulator-Si-substrate (MIS) has been widely used for a long time. Comparing with the simple oxide as a dielectric, the most benefit for high-k dielectrics is the leakage current density reduction by several orders of magnitude at the same Equivalent oxide thickness (EOT). On the other hand, Metal has higher carrier concentrations and lower resistance can replace Si-substrates to reduced the contact resistances and raise the storage charge comparing to normal MIS structure. Due to device shrinkages and the charge storage in conventional MIS structure is hard to meet the requirements, the MIM structure is expected to substitute applied in IC industry.

With the trend of downscaling of MIM capacitors for high capacitance density, thickness of dielectrics must reduce and thus increase undesired leakage current and poor voltage linearity. To go in for high capacitance density and scaling down device, high-k dielectrics have investigated for a while, such as Ta_2O_5 [2], HfO_2 [3], Al_2O_3 [4]. Table 1.1 show the comparison of relevant properties for some high-κ candidates. In the other way, variation of dielectric or MIM structure, like as

sandwich [5] or laminate structures [6](Fig.1.1), had been investigated. In addition, researches of nanodots embedded in insulators shows high dielectric permittivity value in nanoscale MIM device [7], which has advantage in increasing permittivity and decreasing device scale.

1.2 Introduction to FePt magnet nanodot (MND)

1.2.1 FePt magnet nanodot fabrication

The synthesis and assembly of small hard magnetic magnetic nanodot (MND) have attracted more and more attention because of their potential applications in ultrahigh-density magnetic recording [8], ferrofluids [9], advanced nanocomposite permanent magnets, [10][11] and even biological microsystems. The chemically ordered FePt face-centered-tetragonal (fct) phase is an excellent candidate for those applications due to their good chemical stability , high magnetocrystalline anisotropy, *Ku* (~10^8 erg/cm3)[12][13] and and saturated magnetization *Ms*=13.8 kG.

There are two way to prepare the FePt magnet nanodot in generally:

The first method, invented by Sun. [14], it used a combination of oleic acid and oleyl amine to stabilize the monodisperse FePt colloids and prevent oxidation. The synthesis is based on the reduction of $Pt(acac)_2$ (acac-5-acetylacetonate, $CH_3COCHCOCH_3$) by a diol and the decomposition of $Fe(CO)_5$ in high-temperature solutions. The use of diol or polyalcohol (for example, ethylene glycol or glycerol) to reduce metal salts to metal particles is referred to as the "polyol process" [15]. If modified this procedure by using a longchain 1,2-hexadecanediol to reduce the

$Pt(acac)_2$ to Pt metal. Thermal decomposition of $Fe(CO)_5$ has been used to produce Fe particles . Both chemical reactions were initiated together in the presence of oleic acid and oleyl amine, providing a convenient route to monodisperse FePt nanoparticles [16] as show in Fig.1.2

The FePt particle size can be tuned from 3 to 10 nm by first growing 3-nm monodisperse seed particles in situ and then adding more reagents to enlarge the existing seeds to the desired size. These particles are isolated and purified by centrifugation after the addition of a flocculent (for example, ethanol) and can be redispersed in nonpolar solvents in a variety of concentrations. When the FePt colloids are spread on a substrate and the carrier solvent is allowed to slowly evaporate, FePt nanoparticle superlattices are produced.

The another way is developed by Cheng-Kuan YIN [17], FePt MND films that were formed by a novelself-assembled nanodot deposition (SAND) method(Fig.1.3), where FePt pellets lay on the SiO_2 target to cosputtered in the high-vacuum RF magnetron sputtering equipment. The target ratio of FePt/SiO_2 was defined as ratio of the area of FePt pellets to the suface area of a SiO_2 target where the FePt pellets are placed. Therefore, the target ratio of FePt/SiO_2 is controlled by changing the mumbers of FePt pellets. To obtain uniform dot size ans dot density, the silicon substrate was rotated at a rate of 75 rpm during sputtering process. As-deposited FePt nanodots were self-assembled into a chemically disordered face-centered cubic (fcc) phase. Thermal annealing converts the chemically disordered FePt nanodots into chemically ordered fct ferromagnetic FePt nanodots. Annealing was performed in a high-vacuum ambience (1×10^5 Pa) to prevent the oxidation of the FePt nanodots.

1.2.2 Hysteresis loop

When ferromagnetic material is under applied magnetic field, its induced magnetic field is raise according to applied field increasing from zero to maximum. (Fig.1.4)Up to some value, ferromagnetic magnetic field keeps steady whether applied magnetic raise, this value is saturation magnetization (A-point). And then decreasing applied field, the induced magnetic field is also decreasing by another path, not along previous magnetization curve to zero applied field. This is hysteresis phenomenon, and B point is remanence magnetization. At this point, a reverse magnetic direction field is required to demagnetize (C point),this value is coercivity (Hc) or coercive field intensity. As same effect to positive magnetic direction, a reverse magnetic direction also let ferromagnetic material saturated at D point, and when applied force decreasing to zero (E point), the magnetization curve becomes a loop form. The curve is called magnetic hysteresis loop.

1.3 Motive

In past, magnetic material, such as Fe,Co,Ni and their compound ,is regard as pollution in front-end stage fabrication in semiconductor area. There are seldom experiments on magnetic nanodot applied in tradition MIS capacitors. We want to expand to the magnetic material application, and explore to the effect on electric properties. We select FePt as our magnetic nanodot material, because it is good chemical stability, high magnetocrystalline anisotropy, and large saturated magnetization. And the superlattice structure was used to embedded FePt magnetic nanodot in traditional MIS capacitor. Layers with magnetic field dependent permittivity may be attractive for application in magnetic sensors.

1.4 The organization of this thesis

In briefly described this thesis, Chapter 1 depicts the background of research and motivation. In Chapter 2, the simulation was used to model the physics mechanism about magnetic material in dielectric layer. Chapter 3 describes the experiment and structure of the capacitor and introduces measurement equipment. Chapter 4 is the result of electric measurement, and material analysis. Chapter 5 summarizes the conclusions and contributions of this thesis, and provides the suggested directions for further research.

Table 1.1. Comparison of Relevant Properties for some high-k candidates.

Comparison of Relevant Properties for Some High-κ Candidates

Material	Dielectric Constant (κ)	Band Gap E_G (eV)	ΔE_C (eV) to Si	Crystal Structure(s)
SiO_2	3.9	8.9	3.2	Amorphous
Si_3N_4	7	5.1	2	Amorphous
Al_2O_3	9	8.7	2.1[a]	Amorphous
Y_2O_3	15	5.6	2.3[b]	Cubic
ZrO_2	25	5.8	1.2[a]	Mono., tetrag., cubic
HfO_2	25	5.7	1.5[b]	Mono., tetrag., cubic
La_2O_3	30	4.3	2.3[b]	Hexagonal, cubic
Ta_2O_5	26	4.5	0.5[a]	Orthorhombic
TiO_2	80	3.5	1.2	Tetrag. (rutile, anatase)

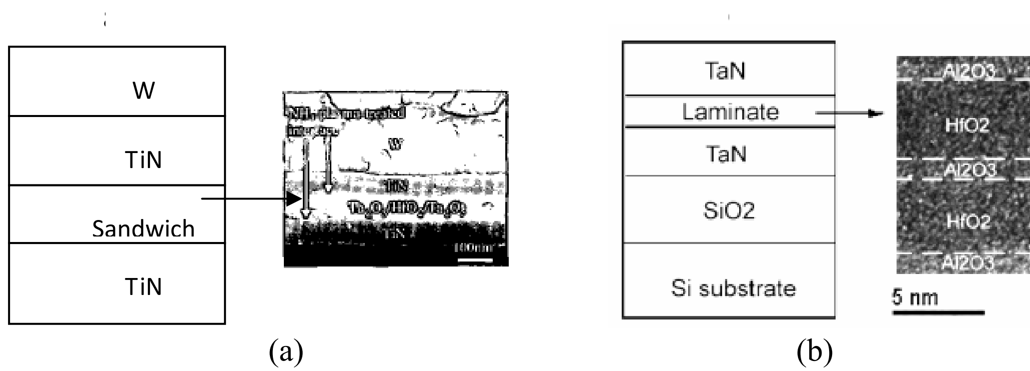

Figure 1.1. Different MIM structure

(a) sandwich MIM[5] (b)laminate MIM structure[6]

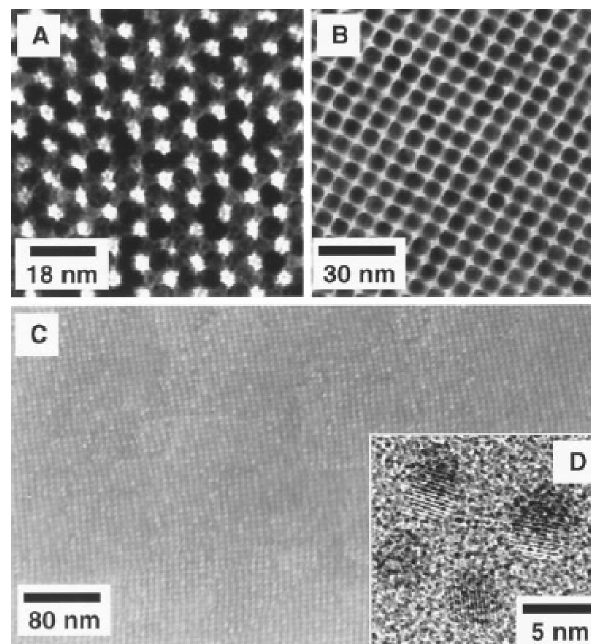

Figure 1.2. (A) TEM micrograph of a assembly of 6-nm as-synthesized $Fe_{50}Pt_{50}$ particles deposited from a hexane/octane dispersion on SiO-coated copper grid nanodot

(B) Replacing oleic acid/oleyl amine with hexanoic acid/hexy-lamine.

(C) HRSEM image after annealed at 560℃ for 30min under N_2 gas.

(D) High resolution TEM image of $Fe_{52}Pt_{48}$ annealed at 560℃ for 30min.[14]

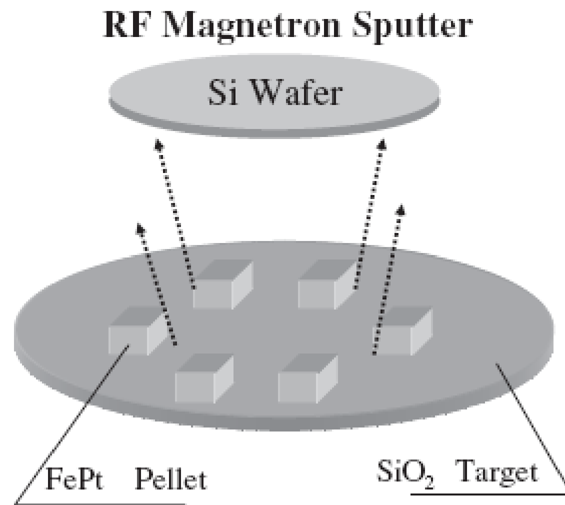

Figure 1.3. Schematic figure of SAND method

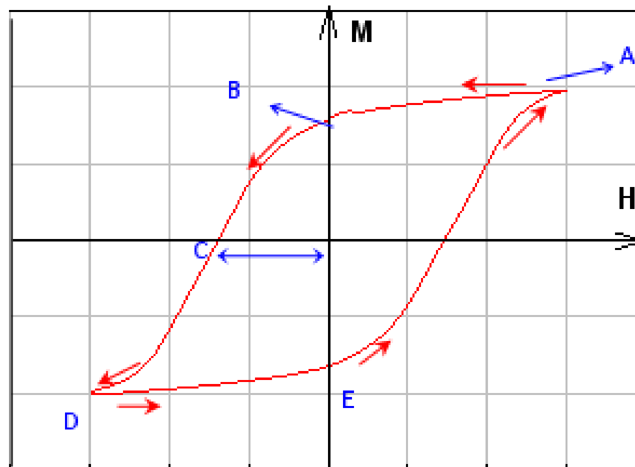

Figure 1.4. Hysteresis loop;

A: Saturation Magnetization: maximum M measured

B: Remanent Magnetization : M at H=0

C: Coercive Field: Field at which M//H changes sign

D: Saturation field

Chapter 2
Experimental details

2.1 Introduction to quantum confinement

The quantum confinement effect can be observed once in the quantum well, quantum wire, or quantum dot which magnitude are the same as the wavelength of the electron wavefunction. When structures scale down to nanodscale, their electronic and optical properties deviate substantially from those of bulk materials. A particle behaves as if it was free when the confining dimension is large compared to the wavelength of the particle. During this state, the bandgap remains at its original energy due to a continuous energy state. However, as the confining area decreases and reaches a certain limit, typically in nanoscale, the energy spectrum turns to discrete. As a result, the bandgap becomes size dependent.

Specifically, the effect describes the phenomenon results from electrons and electron holes being squeezed into a dimension that approaches a critical quantum measurement, called the exciton Bohr radius. In current application, a quantum dot such as a small sphere confines in all three dimensions, a quantum wire confines in two dimensions, and a quantum well confines in one dimension.

The advances in semiconductor technology allow one to go further and fabricate heterostructures in which all existing degrees of freedom of electron propagation are quantized. These are so called quantum-dots, systems are like artificial atoms and they demonstrate extremely interesting behavior. [18]

2.2 Wave functions and energy levels in quantum dots

Quantum-dot is fabricated heterostructure in which all existing degree of freedom of electron propagation are quantized. When considering the spectrum of a zero-dimensional system, we have to study the Schrödinger equation with the confining potential, which is a function of all three coordinates and confines the electron in all three directions [19]. The simplest potential type is

$$V(x,y,z)=\begin{cases}0 & inside\ the\ dot\\ +\infty & outside\ the\ dot\end{cases} \tag{2.1}$$

Where the dot is restricted by the conditions $0\le x\le L_x, 0\le y\le L_y, 0\le z\le L_z$.

(Fig.2.1) The solutions of the Schrödinger equation is

$$\psi_{n_1,n_2,n_3}(x,y,z)=\sqrt{\frac{8}{L_xL_yL_z}}\sin\frac{\pi x n_1}{L_x}\sin\frac{\pi y n_2}{L_y}\sin\frac{rzn_3}{L_z} \tag{2.2}$$

$$E_{n_1,n_2,n_3}=\frac{\hbar^2\pi^2}{2m^*}\left(\frac{n_1^2}{L_x^2}+\frac{n_2^2}{L_y^2}+\frac{n_3^2}{L_z^2}\right) \tag{2.3}$$

Thus we obtain threefold discrete-energy levels and wave functions localized in all three dimensions of the quantum dot. The similarity with atoms is seen another case of spherical dot, the potential is

$$V(r)=\begin{cases}0 & for\ r\le R\\ V_b & for\ r>R\end{cases} \tag{2.4}$$

From quantum mechanics, it is known that under spherical symmetry the solutions of the Schrödinger equation can be expressed by the separation of angular and radial dependences in the form

$$\psi(r,\theta,\phi)=R(r)Y_{l,m}(\theta,\phi) \tag{2.5}$$

, which are the spherical coordinates, the well-known spherical functions, l and m are quantum numbers corresponding to the angular momentum and its projection on axis

z. The Schrödinger equation is

$$\left[-\frac{\hbar^2}{2m^*}\frac{\partial^2 \chi(r)}{\partial r^2}+V_{eff}(r)\right]\chi(r)=E\chi(r) \tag{2.6}$$

$$\text{Where } \chi(r)=rR(r),\ \ Veff(r)=V(r)+\frac{\hbar^2 l(1-l)}{r^2} \tag{2.7}$$

As a result of spherical symmetry, the problem reduces formally to a one-dimensional equation. The energy is a function of two quantum number n and momentum quantum number l, if l=0

$$\psi(r)=\begin{cases} A\sin\frac{k_w r}{r} & k_w=\frac{\sqrt{2m^*E}}{\hbar} \quad r<R \\ B\frac{e^{-K_b r}}{r} & k_b=\frac{\sqrt{2m^*(V_b-E)}}{\hbar} \quad r>R \end{cases} \tag{2.8}$$

At r=R, equations are similar to those studied for one-dimensional problem. We can find an equation (2.9) for the energy

$$\sin k_w R=\pm\sqrt{\frac{\hbar^2}{2m^*V_b}}k_w \tag{2.9}$$

The root shows that a level exists inside the spherical well if

$$Vb\geq\frac{\pi^2\hbar^2}{8m^*R^2} \tag{2.10}$$

Thus, eq(2.10) quantifies that a potential well must be large enough or deep enough to confine the electron.

If l>0, the problem can be analyzed for a large depth of the well. In this case the radial wave functions have the form

$$R(r)=\sqrt{\frac{2\pi k}{r}}J_{l+\frac{1}{2}}(k_w r) \tag{2.11}$$

,where $J_v(r)$ are the bessel function. The roots of the bessel function give us the following series of the energy levels in quantum dots.

2.3 Magnetic field in quantum mechanics

In this section, it is to discuss the quantum structure with magnetic field in quantum electromagnetism. Electron behavior in magnetic field can be described by Schrödinger equation. From the development of formula, quantum confinement and charge localization restrict the charge distribution and improve the insulating behavior (Fig.2.2).

2.3.1 Schrödinger equation with magnetic field [20][21]

The classical Hamiltonian function appropriated for a charged particle (charge q) acted on by external electric and magnetic fields in three dimensions is given by

$$H_{classical} = \frac{1}{2m}\left(\hat{p} - qA(r,t)\right)^2 + q\phi(r,t) \tag{2.12}$$

The corresponding quantum mechanical Hamiltonian is obtained by replacing the momentum variable by its operator counterpart, thereby giving the Schrödinger equation

$$\hat{H}\psi(r,t) = \hat{E}\psi(r,t) = i\hbar\frac{\partial}{\partial t}\psi(r,t) \tag{2.13}$$

$$\text{where} \quad \hat{H} = \frac{1}{2m}\left(\hat{p} - qA(r,t)\right)^2 + q\phi(r,t) \tag{2.14}$$

The classical equations of motion depended on the E and B fields are obviously invariant under any gauge transformation, so the original Hamiltonian is replaced by

$$\hat{H}' = \frac{1}{2m}(\hat{p} - qA(r,t) - q\nabla f(r,t))^2 + q\phi'(r,t) - q\frac{\partial}{\partial t}f(r,t) \tag{2.15}$$

$$\text{where}\; B(r,t) = \nabla \times A(r,t)$$

$$E(r,t) = -\nabla\phi(r,t) - \frac{\partial}{\partial t}A(r,t)$$

For a constant magnetic field B in z-direction, in terms of potentials ϕ and $\vec{A}$, for the interaction of an electron with charge -e and mass μ ,we can take

$$\vec{A} = -\frac{1}{2}\vec{r}\times\vec{B} \tag{2.16}$$

Then, the Hamiltonian from eq.(2.14) can be written as

$$\hat{H} = \frac{\hat{P}^2}{2\mu} + \frac{e}{2\mu}\left(\hat{p}\cdot A + A\cdot\hat{p}\right) + \frac{1}{2\mu}\left(\frac{e\vec{B}}{2}\right)^2\left(x^2+y^2\right) \tag{2.17}$$

The Schrödinger equation takes the form

$$-\frac{\hbar^2}{2\mu}\nabla^2\psi - \frac{ie\hbar}{\mu c}\vec{A}\cdot\nabla\psi + \frac{e^2}{2\mu c^2}A^2\psi + e\phi(r)\psi = E\psi \tag{2.18}$$

And manipulating the 3rd term,

$$\frac{e^2}{8\mu c^2}\left(\vec{r}\times\vec{B}\right)^2\psi = \frac{e^2}{8\mu c^2}\left[r^2B^2 - \left(\vec{r}\cdot\vec{B}\right)^2\right]\psi = \frac{e^2B^2}{8\mu c^2}\left(x^2+y^2\right)\psi \tag{2.19}$$

For a free electron in a static magnetic field, the electron is confined by the potential given by (2.19). This is a 2D harmonic potential, and the allowed energy levels are given by equal spacing according to the harmonic oscillator solutions. These levels are called Landau levels. Depending on both the Landau quantum number N and the magnetic field B, the Lorentz force leads charged carriers to classically describe circular orbits with a cyclotron orbit radius R_N [22]

$$R_N{}^2 = (2N+1)l^2 \tag{2.20}$$

$$\text{where } l = \sqrt{\frac{\hbar}{eB}} = \frac{256\,\overset{0}{\mathrm{A}}}{\sqrt{B}} \tag{2.21}$$

2.3.2 Magnetic field induce quantum confinement

Quantum confinement is another notable issue in magnetic field, since it is strongly related to the Kondo effect [23] and Anderson localization [24], but no microscopic dynamical mechanisms of this phenomenon have yet been understood in detail. However, some experiments prove this phenomenon indirectly, with increasing in-plane magnetic field, an localization in the potential wells of the superlattice

structure increases. Another evidence reveals magnetic field induced electric polarization, charge localization, and insulating behavior [25].

2.4 COMSOL simulation

In this section, we use COMSOL Multiphysics, a simulation of any physics-based system, to simulate the situation of magnetic field effect on multi-wells confined electron. And supposed the constant magnetic field in z-direction like section 2-3-1, we modify eq. (2.19) in Cylindrical coordinates

$$-\frac{\hbar^2}{2m}\left(\frac{\partial}{\partial z^2}+\frac{\partial}{\partial \rho^2}+\frac{\partial}{\rho\partial\rho}\right)u(\rho,z)+\frac{\hbar^2}{2m}\left(\frac{l^2}{\rho^2}+\frac{eBl}{\hbar}+\frac{e^2B^2\rho^2}{4\hbar^2}\right)u(\rho,z)+V(\rho,z)=Eu(\rho,z)$$

where $\psi(x,y,z)=\exp(il\phi)u(\rho,z)$ (2.22)

As description of top formula, with the magnetic field increase, the electron will more easily be confined in the potential wells due to the additional parabolic potential term from magnetic field. Fig.2.3 is the simulation result of 5 quantum wells with width of 2nm, spacing of 2nm, depth of 1.0eV, with the magnetic field increase, the profile of probability density function is narrowing to represent the confinement effect. Altering other parameters, to increase spacing and well width, the probability in center well is increasing.(Fig.2.4,2.5). Moreover, larger effective mass shows lower tunneling probability and better field confinement in Fig.2.6 Besides, the magnetic field in transverse direction suppressed the tunneling probability more efficiently for lower effective mass, lower barrier height, higher bias voltage and wider barrier width(Fig.2.7,2.8,2.9,2.10), this phenomena were from the relation of two constants ($\omega_c$and τ)[20], where

$$\omega_c = \frac{eB}{m^* C} \quad \text{(cyclotron frequency)} \tag{2.23}$$

$$\tau \approx \int \frac{dx}{\sqrt{2[U(x) - E]/m^*}} \quad \text{(tunneling time scale from WKB approximation)} \tag{2.24}$$

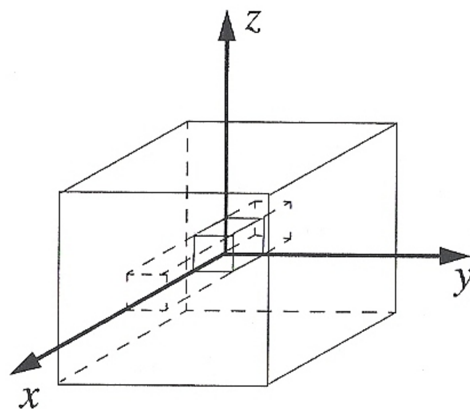

Figure 2.1 Sketch of a quantum box embedded in a matrix

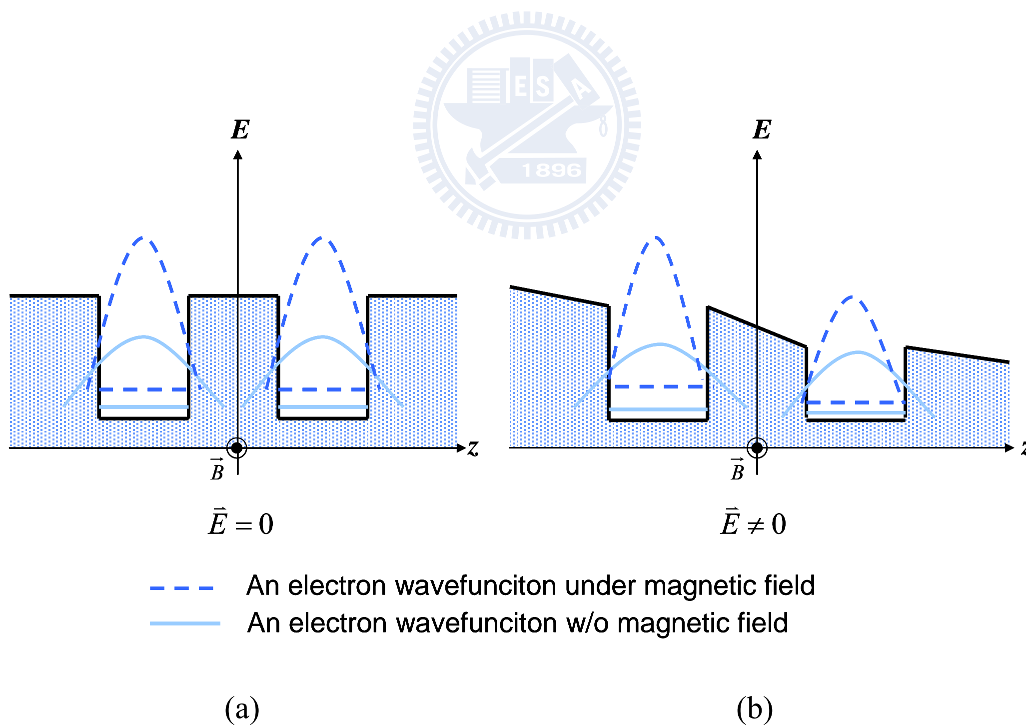

Figure 2.2 Schematic presentation of the wavefunction altered with magnetic field in quantum wells

(a) under magnetic field (b) under electric field and magnetic field

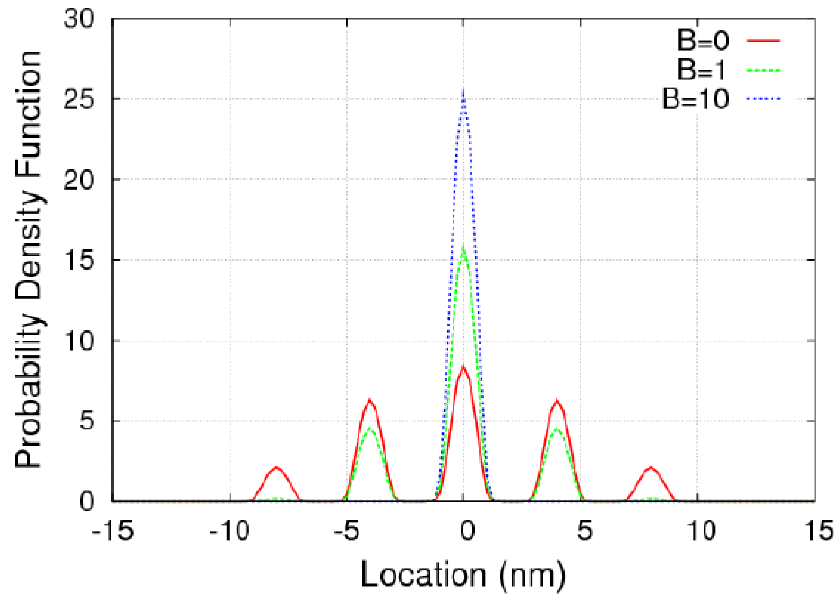

Figure 2.3 five quantum wells with width 2nm, spacing 2nm, depth 1.0eV with ky=0

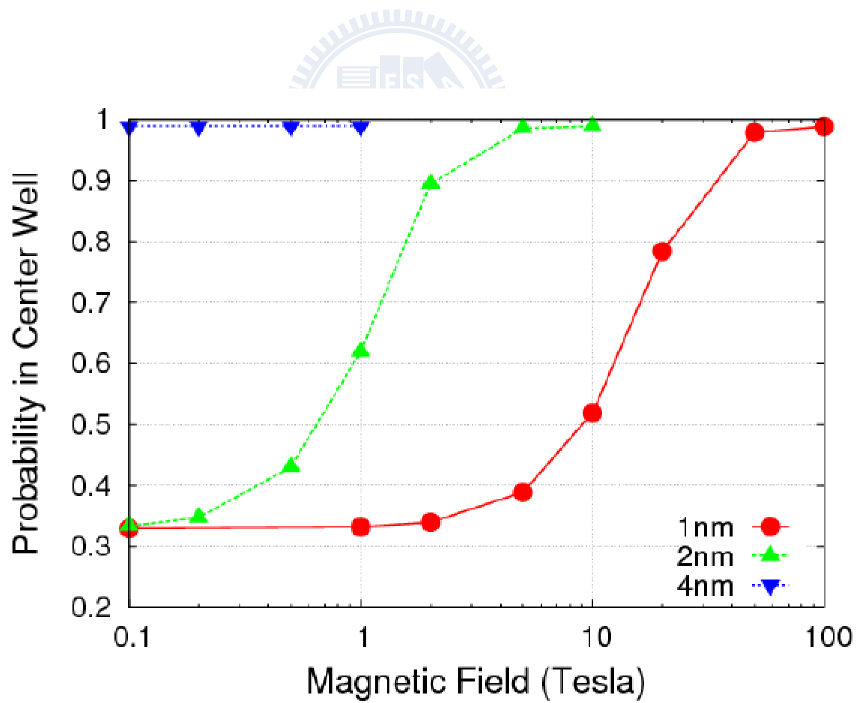

Figure 2.4 Probability in center well with different spacing

in well width 2nm, well depth 1.0eV

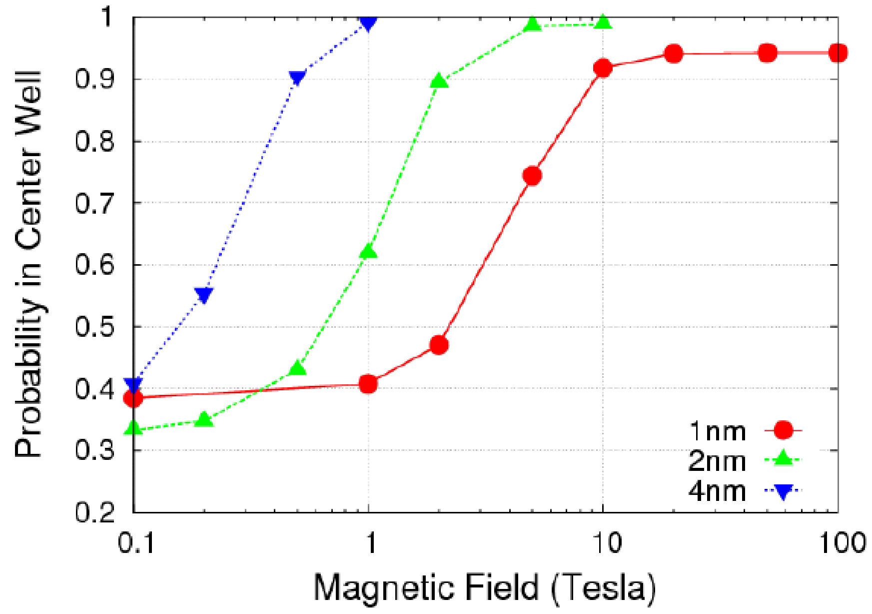

Figure 2.5 Probability in center well with different well width

in well spacing 2nm, well depth 1.0eV

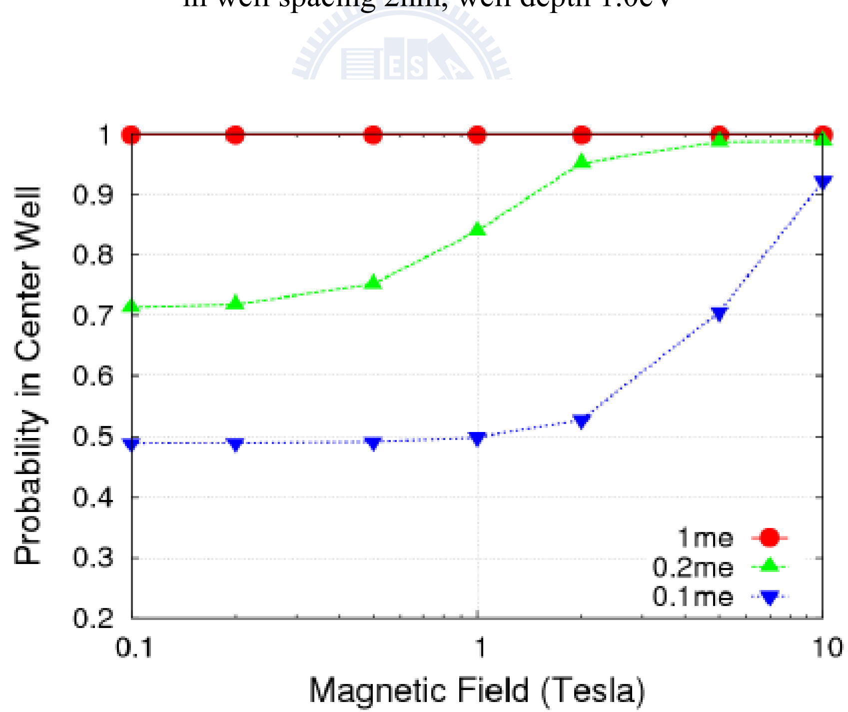

Figure 2.6 Probability in center well with different effective mass

in well spacing 2nm,well width 2nm, well depth 5.0eV

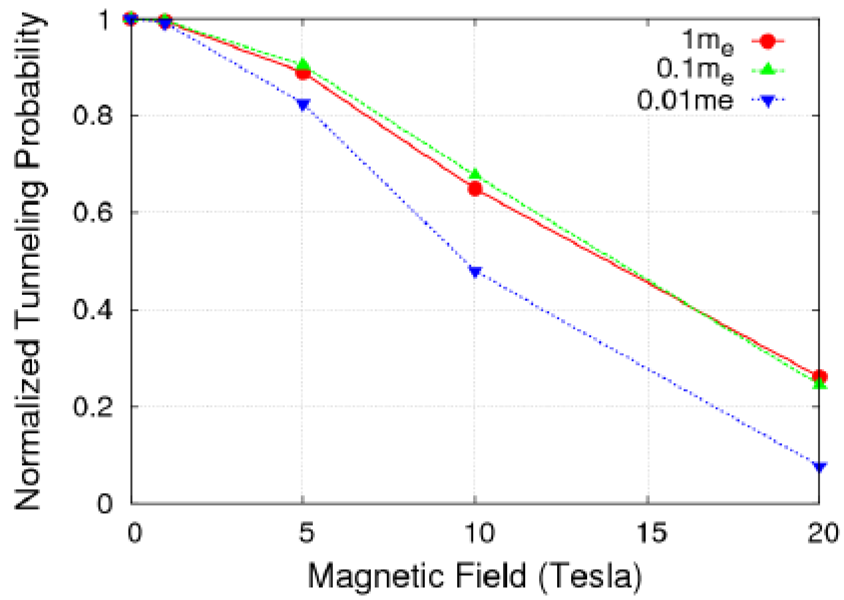

Figure 2.7 The magnetic field can suppress the tunneling probability more effectively with small electron mass

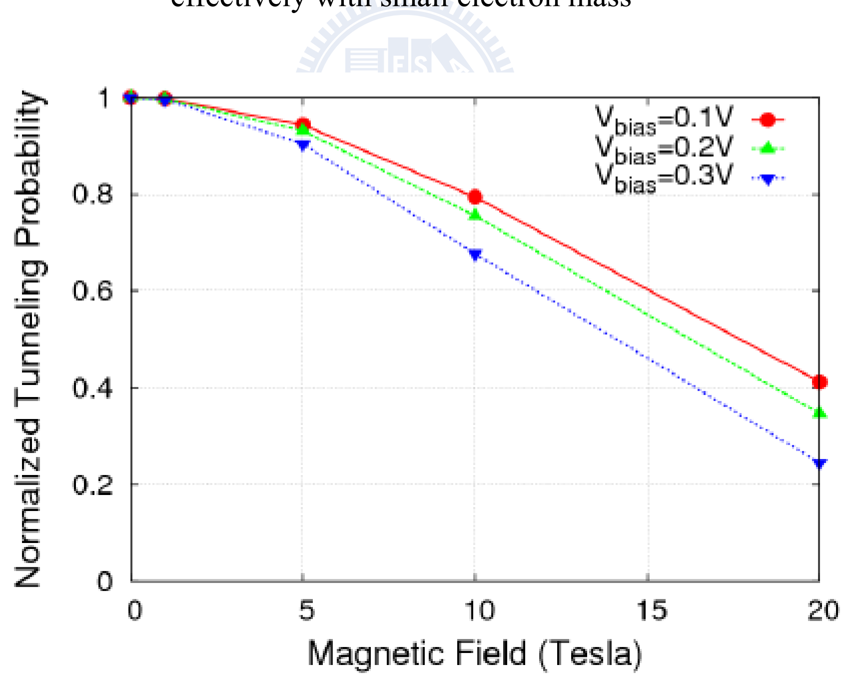

Figure 2.8 The magnetic field can suppress the tunneling probability more effectively with large bias voltage

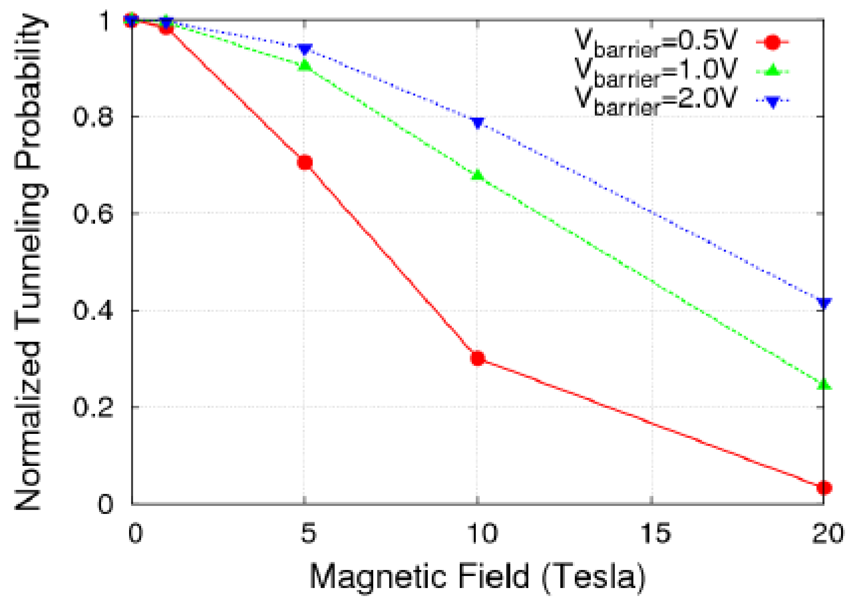

Figure 2.9 The magnetic field can suppress the tunneling probability more effectively with lower barrier height

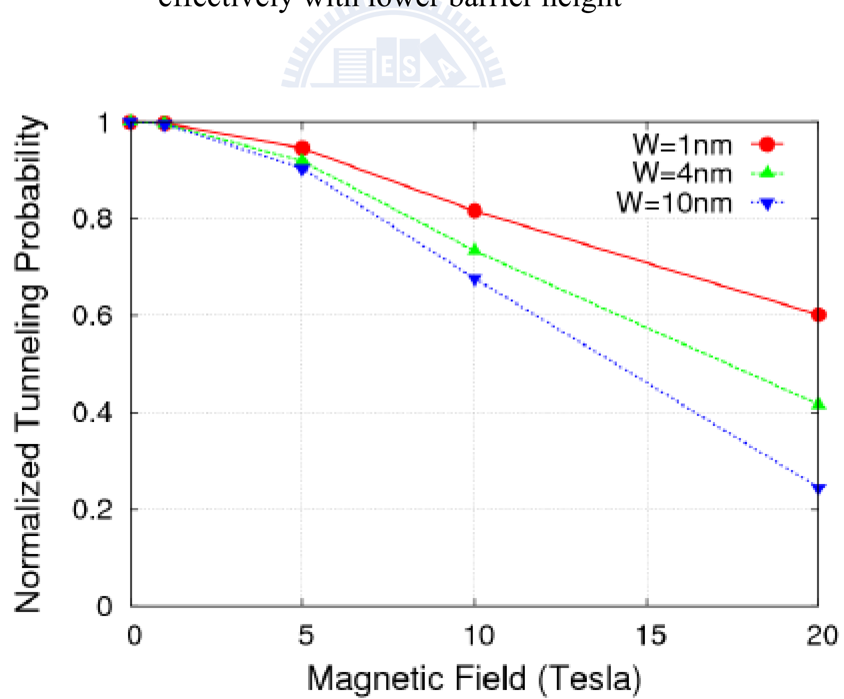

Figure 2.10 The magnetic field can suppress the tunneling probability more effectively with wider barrier width

Chapter 3

Device Structure and Fabrication

In this chapter, first, describe the experiment process with magnet nanodoat (MND) in capacitor mentioned and their fabrications are described in 3.1. Material analysis and electric measurement were introduced in 3.2.

3.1 Magnetic nanodot capacitor Fabrication (Fig.3.1)

Step1. Preparation of Substrate with buffer oxide.

2-inch p-type single crystal silicon wafers with (100) orientation were used as the starting materials(10-15Ω-cm). After an RCA initial cleaning procedure. Si wafers were grown with 10-nm-thickness thermally grown SiO_2 in steam oxygen and hydrogen ambient at 900°C. the SiO_2 layer is play a role of insulating layer avoiding current leakage from the Si substrate.

Step2. FePt magnetic nanodot layer

Magnetic nanodots are formed by RF magnetron sputter. In this step , we use self-assembled nanodot deposition (SAND method) [26], our target is SiO_2 with FePt pellet, flow 8 sccm Ar gas and drive power 50W and deposition rate is less than 0.1 Å. Low power and low pressure is necessary to control the nanodot to form within SiO_2 layer and exactly in thickness 10nm. Another comparison sample, embedded in Co nanodot.

Step3. Preparation of interlayer insulator block oxide .

It is the same way that use RF magnetron sputter with Ar gas flow 8 sccm.

Power descend to 50W to drive the plasma to pure SiO_2 target for lower deposition rate in order to grow only 3nm thickness SiO_2 as block oxide between FePt magnetic nanodot layer. Block oxide can avoid FePt magnetic nanodot diffusing.

Step4. Cycle deposition for superlattice structure..

After setp3, repeat step 2 and step 3 in seven cycles for superlattice structure.

Step5. Vacuum annealing .

Vacuum annealing under pressure 5×10^{5} Pa, 700℃, 30min. This step transforms FePt fcc structure to fct structure ($L1_0$). During the post-heat-treatment, the heat is supplied only from the bottom side of the substrate. For a given annealing temperature and time, the quantity of heat transferred to the FePt-dot layer is larger for a thin 2.5 nm block oxide as compared to that for a thicker 10 nm block oxide. This results into an increase in the size of the nanodots in the sample with a thinner block oxide. The core of the as-formed FePt nanodots was always preserved in the metallic state. Possibly, the high vacuum ambient during postannealing, which is inevitable to transform the as-grown fcc structured FePt nanodots which is nonmagnetic into the magnetically hard $L1_0$ structured one, highly promotes the release of oxygen from the metal oxides of FePt nanodots via reduction reaction. This leads to not only an increase in the fraction of metallic Fe and Pt at the periphery of FePt nanodots, but also the formation of a high quality SiO2 matrix.

Step6. Preparation of top electrode and bottom electrode

In order to define electrode area on wafer, we use shadow mask was used to paste on wafer surface and coat Al 400nm by thermal coat. Top electrode size is from $0.00504cm^2$~$0.0003cm^2$. Bottom electrode is also Al 400nm back-coating on wafer.

3.2 Material analysis and Electric measurement

The magnetic moment is measured by Vibrating Sample Magnetometer (VSM) (Fig.3.2). When a sample is under single direction magnetic field, it will has induced magnetic moment. If sample vibrates like sin wave mode under magnet winding, the magnetic flux changes with vibration. It was detected by another magnet winding, and induced signal voltage. This signal is in proportional to magnetic moment and measure magnetic characteristic. In VSM, every sample is under addition magnetic force 30kOe (±15kOe) and vibration frequency 80Hz. The smallest detective magnet is 5×10^{-5} erg/Oe. Therefore Coercive field and saturation field can be known from magnetic hysteresis loop.

Structure and morphologies of cross section were confirmed by transmission electron microscope (TEM) in Fig.3.3 X-ray diffraction (XRD) was employed to identify the crystal structure of the nanodot using Cu Kα radiation with λ=0.5418 nm. And check the components of FePt ratio were estimated by inductively coupled plasma-mass spectrometer (ICP-MS).

For electrical measurement, the leakage current-voltage (*J*-*V*) curves were measured by the semiconductor parameter analyzer of model Kethley 4200. The capacitance-voltage (*C*-*V*) curves were measured by the precision impedance meter of model Agilent 4284A.

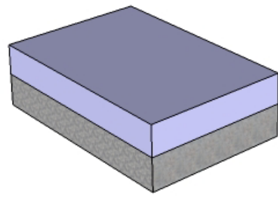

(a) step1:RCA clean and LPCVD 10nm

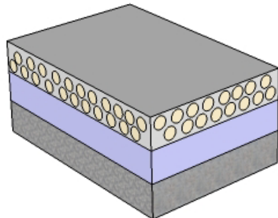

(b) step2:FePt nanodot with SAND method

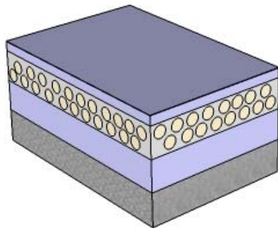

(C) step3:Sputter 3nm block oxide

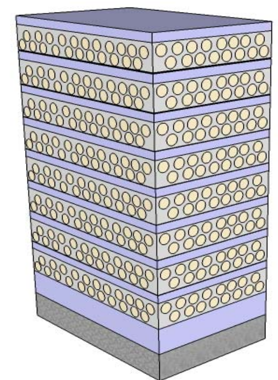

(d) step4:Repeat step2~step3 ,total 8 cycles

Step5: Vacuum annealing 700 ℃

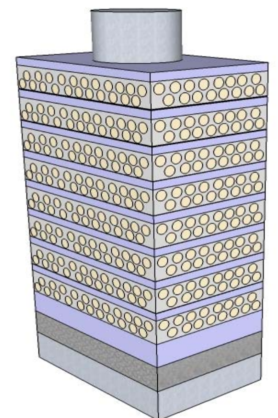

(e) step6: Top and bottom coat Al electrode

Fig. 3.1 The process flow (a)stpe1 (b)step2 (c)step3 (d)step4 (e)step6

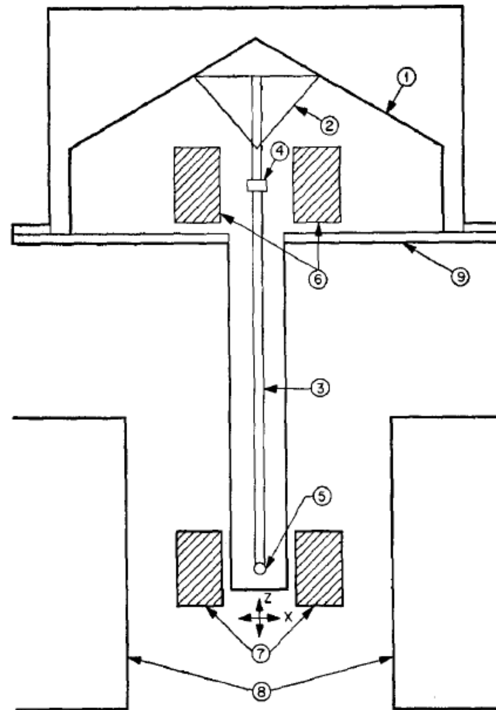

Fig. 3.2 Vibrating Sample Magnetometer (VSM) structure (1) Loudspeaker transducer (2) conical paper cup support (3) drinking straw (4) permanent magnet reference sample (5) sample (6) reference coils (7) sample coils (8) magnet poles (9) metal container to allow evacuation.

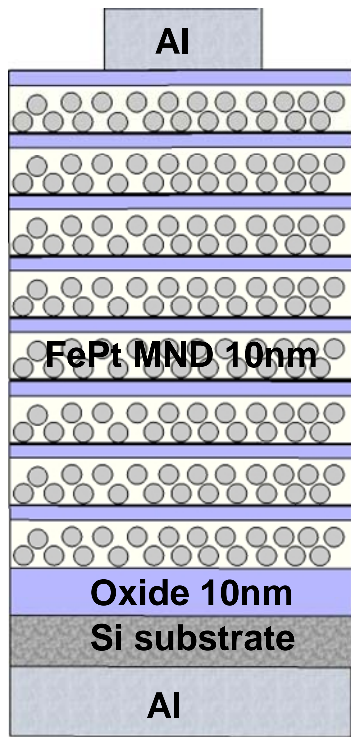

(a)

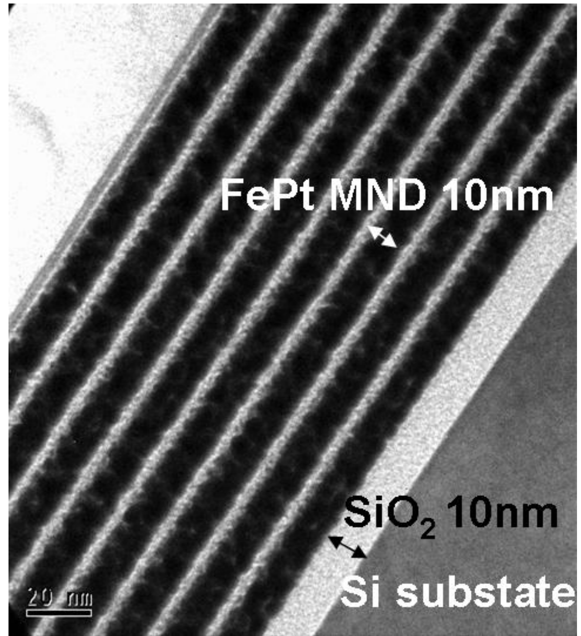

(b)

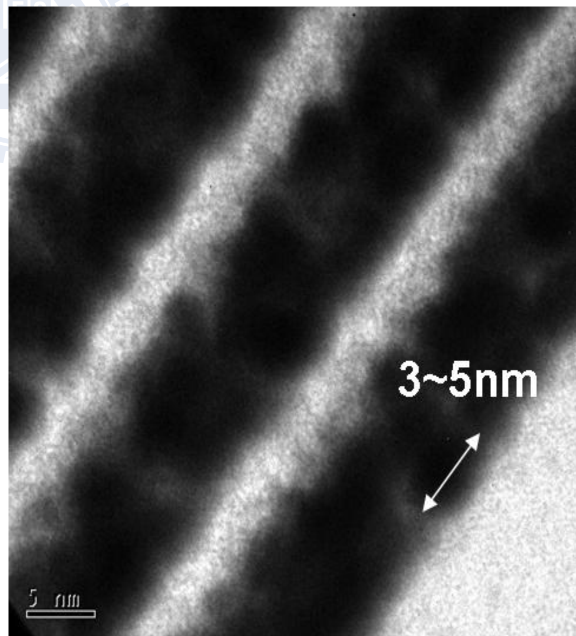

(c)

Figure 3.3 Transmission electron microscope(TEM) morphology of cross section (a)cross structure (b)scale 20nm (c)scale 5nm

Chapter 4

Experiment Results and Discussion

4.1 The magnetic FePt film properties

In order to confirm FePt to have magnetic properties, we try to find the best FePt magnetism characteristic. We change different atomic concentration Fe:Pt ratio in the way of altering film thickness during sputtering, try different annealing condition, measure the magnetization moment by VSM and compare with paper [27] in $L1_0$ *fct* lattice structure in XRD see Fig.4.1 After annealing in vacuum, the FePt lattice structure transforms from original *fcc* to *fct*. The annealing temperature need to reach to 600℃ to transform its structure, and the evidence is that peaks appear after the 600℃ 30 minutes annealing. However, below 600℃ it stays *fcc* state without any direction of *fct* structure. Fig.4.2 is the VSM of the different Fe to Pt ratio with vacuum annealing 600℃ 30 minutes, the magnetic property of FePt is not only decided by its *fct* structure, proper ratio of the number of Fe and Pt atoms is also the major factor. Beside, the under layer and annealing temperature also play an important role to arrange the Fe and Pt in correct order and with large magnetic anisotropy. Fig.4.3 is the effect of magnetism on different under layer. For Pt as being the buffer layer, it can order the growth of FePt *fcc* phase extended into the $L1_0$ FePt (001) magnetic layer [28], which can be not only exhibited a large parallel magnetic field but also used to bottom electrode. Pt under layer has another advantage for high stability in heat treatment and metal addition [29]. On the topic of Fe:Pt ratio, we quantitatively determine by layer thickness, and exactly analysis component ratio by inductively coupled plasma mass spectroscopy (ICP-MS). Seeing Table 4-1. the

elemental percentage of Fe:Pt = 48:52 has large coercivity and saturation magnetization. Fig 4.4 is the magnetic hysteresis loop of FePt MND MIS capacitor after magnetic annealing 700℃ 60 minutes. Table 4-2 is the physical quantity value of magnetic field.

4.2 Properties of magnetic nanodot MIS leakage characteristics

To recognize the effect of magnetic nanodot in capacitor, we measure the characteristic of current density and voltage. Fig.4.5 shows the current density verse voltage of magnetic FePt nanodot MIS capacitor with different Al top electrode area. Asymmetry curve reveals different leakage mechanism in two current directions. When positive bias force on $3 \times 10^4 \mu m^2$ Al top electrode, the leakage curve is flat to 9.5×10^{-5} A/cm under ±10V. This is the value that electrons overcome the 10nm block oxide barrier on Si. Beyond +10V, leakage current density increases quickly to 10 A/cm and is not breakdown even under high voltage strength 100V. In this region, MIS capacitor with FePt MND (magnetic nanodot) is with high leakage current which is unusual in MIS capacitor without MND. On the other way, reverse bias force on top electrode, the leakage current also has the same behavior in first -10V. If negative bias is larger than this value, the leakage current mechanism is different. To recognize the leakage current mechanism of the magnetic nandot capacitor, we take five different mechanisms into consideration (see Table 4-3) [30].

4.2.1 Ohmic Conduction Fitting

For the leakage current at very low field (~±10V in MND FePt capacitor), the leakage current in accumulation mode increases linearly with the increase of voltage bias as shown in Fig.4.6(a). The red line is presents a fitting curve of Ohmic

conduction mechanism, which describes the situation of low voltage and high temperature, current is carried by thermally excited electrons hopping from one isolated state to the next. Ohmic conduction takes place when the injected carrier density is far less than the thermally-generated carrier density, which thermally–generated carriers are dominant in conduction. The relation can be expression in (4-1)

$$J = aV\exp\left(-\frac{c}{T}\right) \tag{4-1}$$

Where *a, c* is constant, *V* is applied voltage and T is the absolute temperature. We can also observe from Fig.4.6(b), a plot of *J* verse *V* yields a straight line within +10V (depletion mode). When applied voltages are between 10 to -10V, the carriers transport mechanism is Ohmic conduction.

4.2.2 Schottky Emission Fitting

Fig.4.7(a) shows the Schottky emission fitting for FePt nanodots MIS capacitor in accumulation mode. The linear relationship of $ln(J/T^2)$ versus $V^{1/2}$ curve was obtained in the range of -25V to -40V, which gives the slope of 2.504 $eV(m/V)^{1/2}$ with a goodness of fit functions of 0.9965. The fitting curve in depletion mode is in the range of 13V~20V. Schottky emission mechanism is which leakage current contributed by the carriers that overcome the barrier height between electrodes and dielectric layers, it is also called thermionic emission because the key point is hot carrier emission jump across barrier height. The formula is below:

$$J = A^{*}T^{2}\exp\left[\frac{-q(\phi_B - \sqrt{qE/4\pi\varepsilon})}{kT}\right] \tag{4.2}$$

Where A^* is the Richardson constant, k is the Boltzmann's constant, T is the absolute temperature (K), E is the applied external electric field , e is electron charge, ε is the permittivity in vacuum, and φ_B is corresponding to the barrier height between metal/dielectric. Fig.4.7(b) is the thermal relationship of $ln(J/T^2)$ and $1/kT$, however, extract the slop verse sqrt voltage in Fig.4.8, nonlinear relation between -25 to -49V demonstrates that the leakage current is independent of temperature. Indirectly prove that Schottky emission conduction is not the main mechanism in high field strength.

4.2.3 Frenkel-Poole Emission Fitting

Fig.4.9(a) is Frenkel-Poole emission fitting on reverse bias applied on top Al electrode. Frenkel-Poole emission describes the process for carriers to overcome the barriers resulted from the defect states in dielectric layer, and the barrier lowering is lower in Schottky emission and tunneling. Because its conduction process depends on carrier trapped and detrapped behavior, electric field plays a more important factor than temperature in this mechanism which is verse in Schottky emission. The relationship can be written as following:

$$J = BV \exp\left(\frac{-q\left(\phi_t - \sqrt{qV/\pi\varepsilon}\right)}{kT}\right) \tag{4.3}$$

Where B is material constant, φ_t is trap barrier height, and other parameters are the same as those in Schottky emission. The goodness of fitting curve is reach 0.99 in the range of -12V~-20V, and Fig.4.8 shows the thermal relationship of Frenkel-Poole emission, from the slop of $ln(J/V)$ and $1/kT$ (Fig.4.9(b)), we can figure out the barrier height is 0.049eV from Fig.4.10. It can explain the main mechanism that electrons transport in high electric field is in trap state, which is suspected of not

only in oxide but also produced by embedded FePt nanodot. The magnetic of nanodot may provide another force to induce electron conduct through adjacent traps in quantum mechanics effect. That is the reason that capacitor with FePt nanodot has high breakdown voltage nearly 49.2V when reverse bias force on top electrode, which is extremely large than general in dielectric thickness ~34nm (see TEM section monograph in Fig 3.3), it also reveals that electric field strength in dielectric layer is large to 14MV/cm,

$$E = \frac{V}{t_{ox}} = \frac{49.2V}{34nm} = 14MV/cm \tag{4.4}$$

Compare with non-MND capacitor in Fig.4.11, it shows the J-V characteristic of MIS capacitor compares with FePt MND and non-MND in 38nm oxide thickness. Obviously, with the same oxide thickness, magnetic nanodot FePt enhances the electric field intensity in oxide and high voltage breakdown.

4.2.4 Space Charge Limited Current Fitting

Another leakage mechanism is space charge limited current (SCLC), which is attributed to defects in dielectric under high electric field. After charge injection from an electrode, the space charges are formed by trapped carrier. The major SCLC divided into two parts in following:

$$J = \begin{cases} \theta \dfrac{9\varepsilon\mu V^2}{8d^3} & \theta \ll 1 \\ \dfrac{9\varepsilon\mu V^2}{8d^3} & \theta \gg 1 \end{cases} \tag{4.5}$$

J is current density ,θ is the ratio of free electron to trapped electron , ε is insulator permittivity, d is the film thickness. The current for the unipolar trap-free

case is proportional to the square of the applied voltage. The fitting result in Fig.4.12, the slop in accordance with SCLC mechanism must be 2, but our fitting slop is in proportional line with slope 0.94 from -0.3 to -11V, is less similar fitting in comparison to Ohmic conduction. But in the depletion mode, the bias large than +13V has large fitting goodness 0.991 and slop 1.75 for slop *lnJ* verse *lnV*. In high electric field condition, the gate leakage current in the deep depletion region is mainly limited by the generation of minority carriers via the interface states and bulk traps in the depletion region [31], which results in a lower saturation current level under positive bias. In the standard capacitor without FePt NMD, its leakage current saturated at 10^{-6}A over 40V.

4.2.5 Tunneling Fitting

Electron tunneling through thin dielectric layer is another conventional way to conduction electron, Fig.4.13 is the tunneling fitting curve, which is evidently to observe the relationship of following formula between -13V to before breakdown:

$$J \propto \xi^2 \exp\left[-\frac{4\sqrt{2m^*}(q\phi_B)^{3/2}}{3q\hbar\xi}\right] \propto V^2 \exp\left(\frac{-b}{V}\right) \quad (4.6)$$

Where ζ is the electric field in insulator, m^* is the effective mass, ϕ_B is the barrier height, and V is the applied voltage. We can calculate ϕ_B is 1.07eV in accumulation mode. Obviously, the leakage current of FePt NMD capacitor is not only direct tunneling under high electric field but also transport carriers by jumping or trapping in FePt NMD layer.

Above of all, the leakage mechanism of MND is apparent difference in positive and reverse bias. In reverse bias (accumulation mode), low electric field

(<10V), the carrier transition is Ohmic conduction because FePt nanodot embedded in oxide which made dielectric metalize in carrier conduction properties. Beyond -10V, its current density rapidly rise than before and keep high current density in high field strength until to 49V breakdown. This phenomenon is resulting from FePt MND induced parallel magnetic which attract carrier and restrict their conduction path by quantum confinement localization [32]. The mechanism makes leakage current behaviors obey to like Frenkel-Poole emission and tunneling compound features in high field strength in accumulation mode. FePt nanodots in capacitors are the quantum well location which potential lower than oxide. Additionally, the self-induced parallel magnetic field suppresses the tunneling between adjacent wells in FePt nanodot/SiO_2 layer by layer structure, which results in the electric field strength must be larger than standard situation in order to prompt carriers tunneling. These reasons make carrier conduction is like metallic Ohmic conduction mode in low field, trapped or detrapped mode in high electric field. In positive bias applied on top electrode (depletion mode), the leakage current mechanism is also like Ohmic conduction in 0V~+10V, +10~14V is dominated by Frenkel-Poole emission and higher 14V, it is space charge limited current and restricted by minority carrier concentration from depletion region, keep static leakage level until to +100V. Fig. 4.14 is the total fitting result of FePt MND capacitor in accumulation mode and in depletion mode, respectively.

4.3 The Voltage and Temperature Effect of FePt MND Capacitors

The properties of stability, precision, and endurance are important for capacitors. In this section, we investigate the stress behavior on electrical properties and capacitance variation under constant voltage stress test and different thermal

stress.

4.3.1 Voltage Stress on FePt MND Capacitor

Fig.4.15 shows the leakage current density under +20V stress verse stress time for FePt NMD capacitor. Fig.4.16 and Fig.4.17 show the J-V and C-V behavior after constant voltage stress at 20V for various stress time. In generally, the capacitance density will increase under lower electric field with the increase of stress time since the injected charges pile up in dielectric thin film near top electrode, at meantime , the charge pile-up cause lower electric field to reduce the leakage current at lower voltage because of electron trapping phenomenon in insulator layer. [38] Conversely, an excessive voltage could increase the charges-injected energy largely to damage the dielectric and generate hole traps which decrease the capacitance density and increase the leakage current, respectively. [39]

These phenomena existing in FePt MND capacitor are different. After high voltage stress at 20V, the leakage current keeps static values of 4.5×10^{-5} A and 5.8×10^{-5} A at -10V and +10V, respectively, during stress time (Fig.4.17). A slight variation of leakage current is that leakage current density reduced with increasing stress time in the range from -10 to -15V. FePt nanodots embedded in oxide may attract charge pile-up, it could result from FePt providing a lower potential position to receive the charges and confinement these charges that reduce the leakage current with increasing stress time. The capacitance density increases with the increase of stress time since the injected charges pile up at FePt nanodots and oxide matrix interface. After the existing traps were filled by the injected electrons, electrons tunneled through the dielectric layer easily so that few electrons were trapped but many new traps were generated in the bulk of dielectric by the high energy electrons.

. Therefore, capacitance density increased because of the new dipole formation

due to the piled-up electrons.

4.3.2 Thermal Stress on FePt MND Capacitor

Fig.4.18(a) shows capacitance density of the FePt MND capacitor at 1MHz from 25℃ to 125℃. After thermal stress, the capacitance density increases with temperature at 1MHz and more obviously at 1KHz (Fig.4.18(b)). The major reason is considered to be the interface defect density existed between FePt nanodot and oxide matrix medium increasing during the thermal stress process. The leakage current density also affected on thermal stress in depletion mode, it can reveal that FePt nanodot structure is relatively stable under thermal stress in accumulation mode. Fig.4.19 shows the effect on current density with thermal stress. In accumulation mode, current density increases slightly with temperature before breakdown voltage. In depletion mode, current density increases nearly one order in magnitude beyond +13V on the rise per of temperature per 25℃. It is worth noting that current density did not rise when temperature exceed 100℃. As mentioned previously, carrier conduction is major limited by the generation of minority carriers via the interface states and bulk traps, and the generation and recombination rates of minority carriers are proportional increasing with temperature. [40]

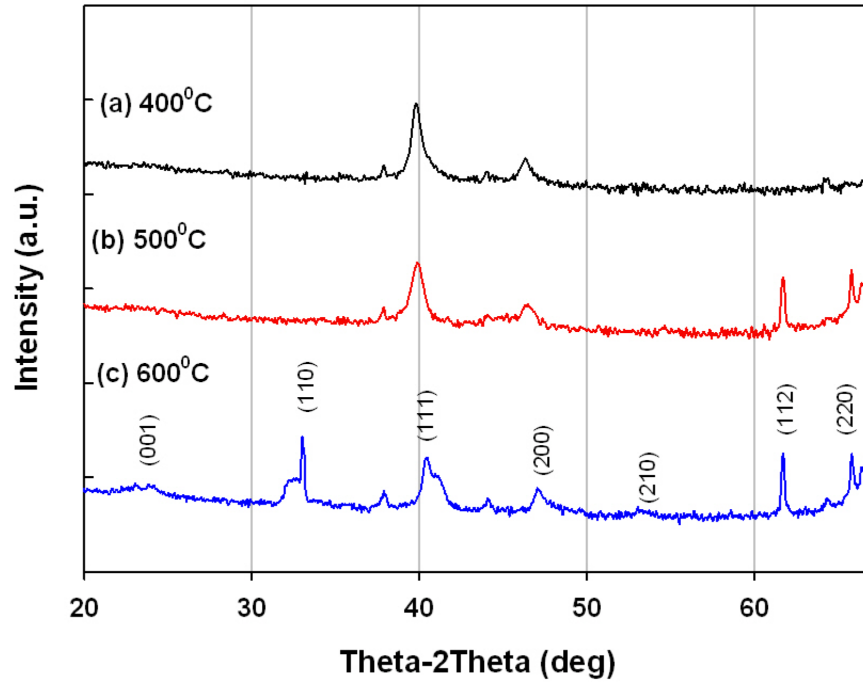

Figure 4.1 XRD pattern of FePt thin film with different annealing temperature for 30min (a)400℃ (b)500℃ (c)600℃

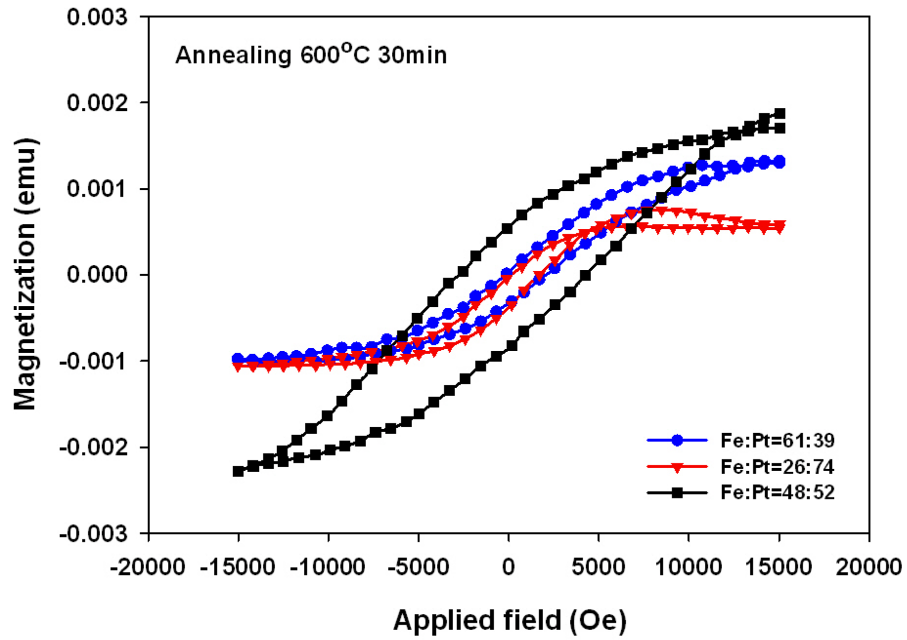

Figure 4.2 Magnetic hysteresis loop of FePt thin film parallel magnetic field with different element ratio

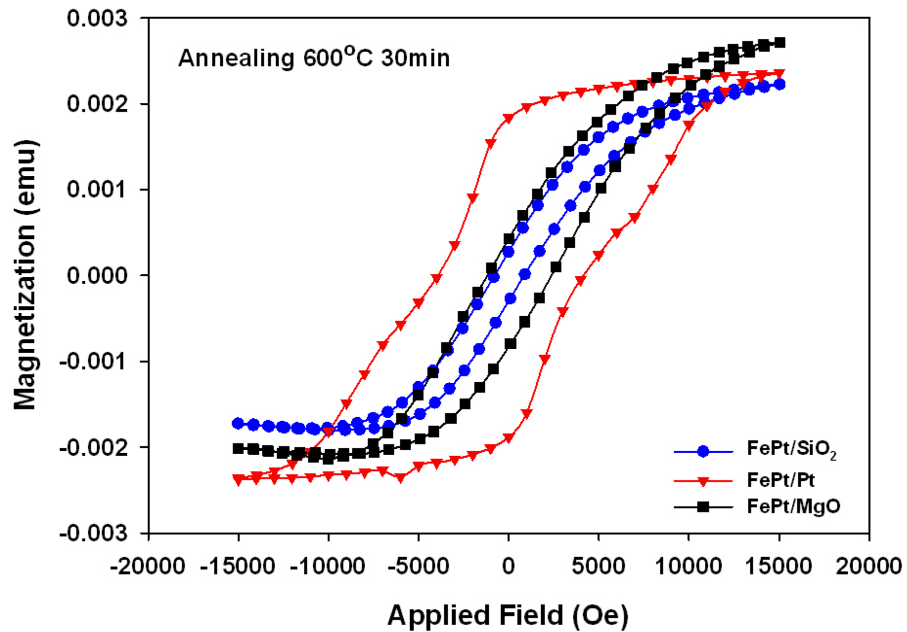

Figure 4.3 Magnetic hysteresis loop of FePt thin film fabricate on different underlayer

Table 4-1 Different element concentration ratio of Fe:Pt measured by ICP-MS

Estimative ratio by thin film thinkness (Å)	Real ratio (ppm)	
Pt:Fe	Pt	Fe
25:20	0.7114(26%)	2.0246 (47%)
25:25	0.657(39%)	1.040 (61%)
51:40	2.764(53%)	2.432(47%)
51:40	0.577 (48%)	0.617(52%)

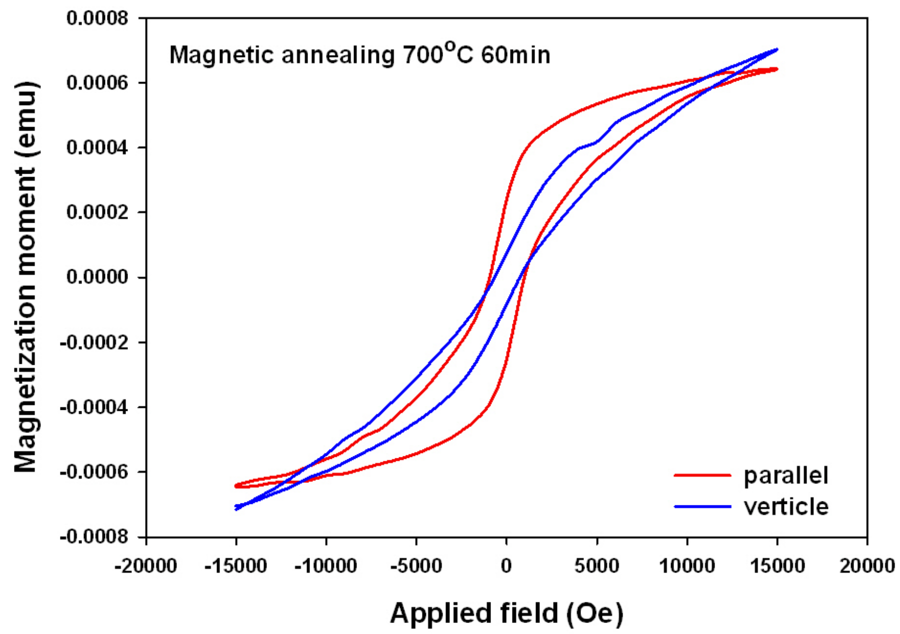

Figure 4.4 Magnetic hysteresis loop of MND MIS capacitor after magnetic annealing 700℃ 60 minutes

Table 4-2 Magnetization value of FePt MND Magnetic hysteresis

Physics quantity (unit)	**Parallel magnetic field**	**Vertical magnetic field**
Ms(emu)	6.433×10^{-4}(0.26T)	7.086×10^{-4} (0.29T)
Mr(emu)	2.457×10^{-4} (0.1T)	7.854×10^{-5}(0.03T)
Hs(Oe)	12724.86	13846.89
Hn(Oe)	10271.99	13414.54
Hc(Oe)	968	716.46

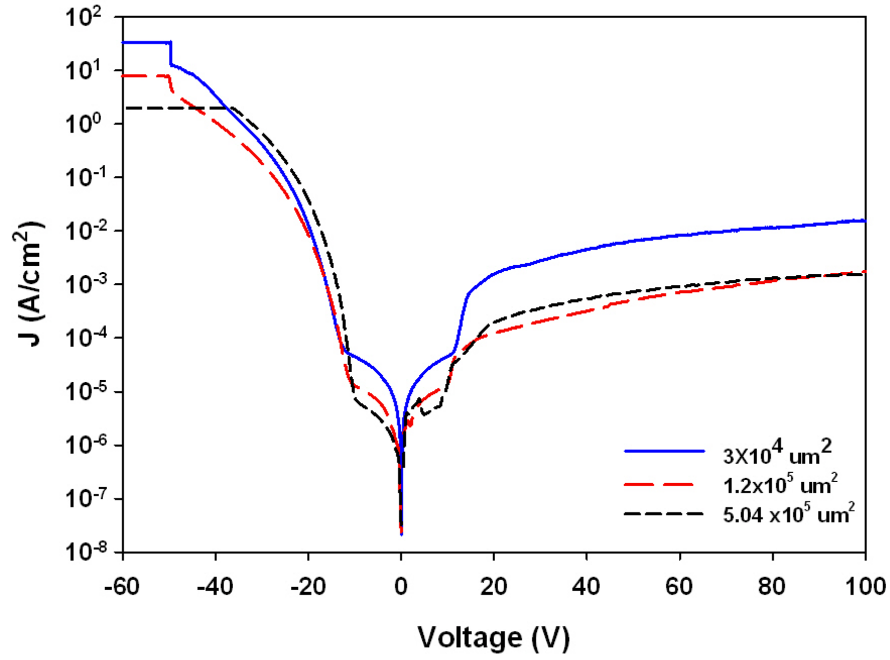

Figure 4.5 *J-V* ofmagnetic FePt nanodot MIS capacitor with different Al top electrode area

Table 4-3 Cnduction mechanisms[30]

Conduction mechanism	Characteristic	Temperature dependence	Voltage dependence
Tunneling	$J \propto \xi^2 \exp\left[-\frac{4\sqrt{2m^*}(q\phi_B)^{3/2}}{3q\hbar\xi}\right]$	None	$\ln\left(\frac{J}{V^2}\right) \sim \frac{1}{V}$
Termionic emission (Schottky emission)	$J = A^*T^2 \exp\left[\frac{-q(\phi_B - \sqrt{qE/4\pi\varepsilon})}{kT}\right]$	$\ln\left(\frac{J}{T^2}\right) \sim \frac{1}{T}$	$\ln J \sim V^{1/2}$
Frenkel-Poole emission	$J = BV \exp\left(\frac{-q(\phi_t - \sqrt{qV/\pi\varepsilon})}{kT}\right)$	$\ln\left(\frac{J}{V}\right) \sim \frac{1}{T}$	$\ln\left(\frac{J}{V}\right) \sim V^{1/2}$
Ohmic	$J = aV \exp\left(-\frac{c}{T}\right)$	$\ln\left(\frac{J}{V}\right) \sim \frac{1}{T}$	$J \propto V$
Space-charge-limited	$J = \frac{9\varepsilon_i \mu V^2}{8d^3}$	None	$\propto V^2$

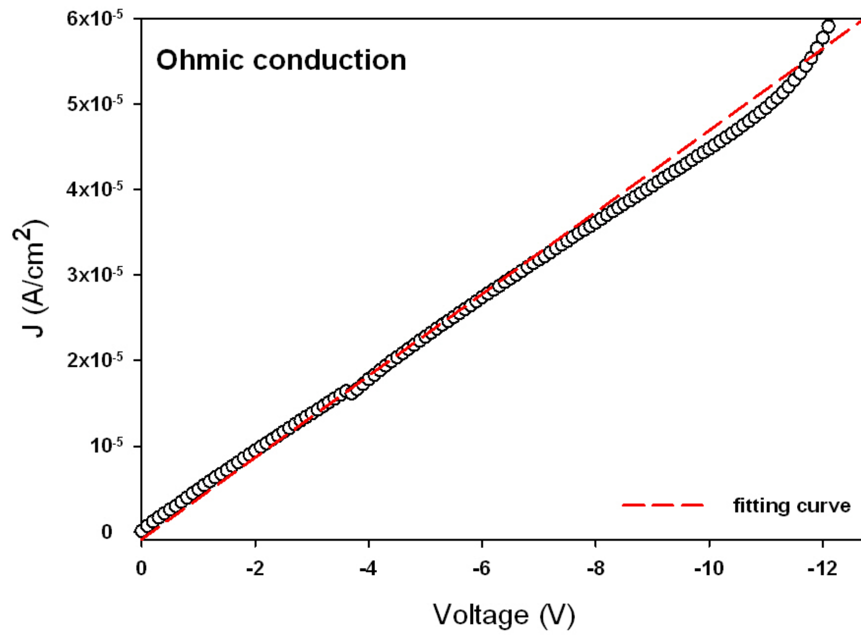

(a)

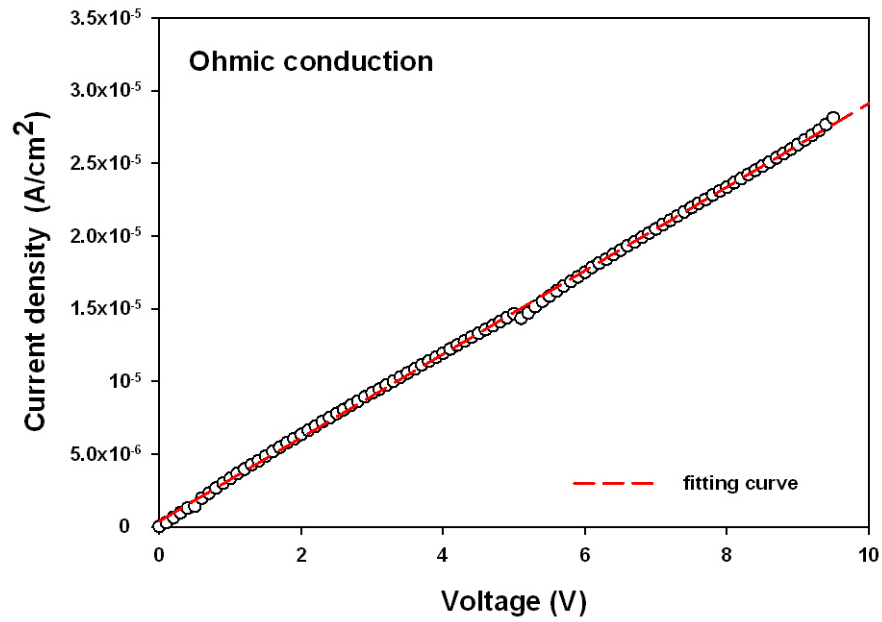

(b)

Figure 4.6 Ohmic Conduction Fitting (a)accumulation mode (b)depletion mode

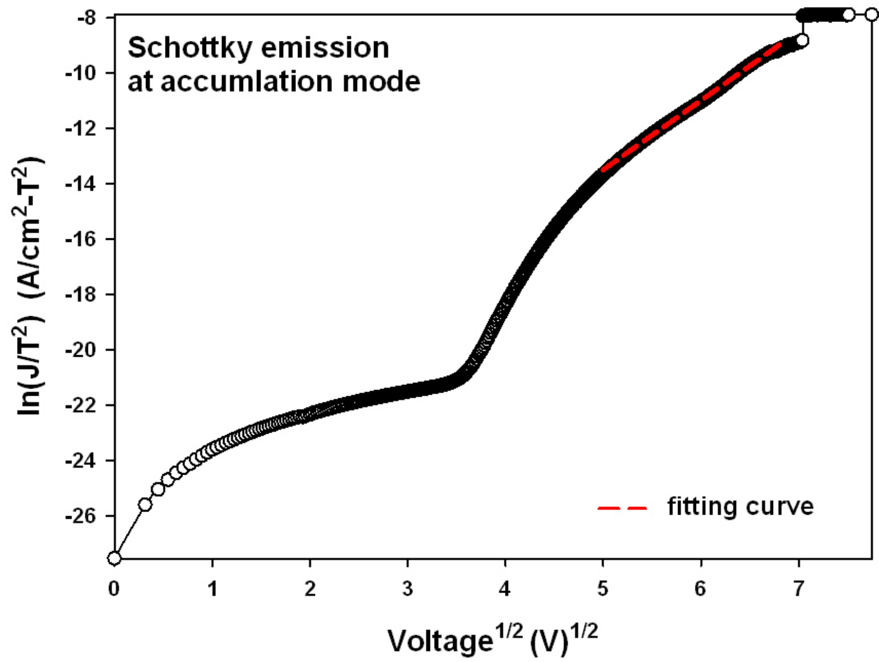

(a)

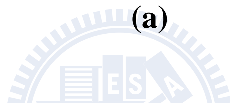

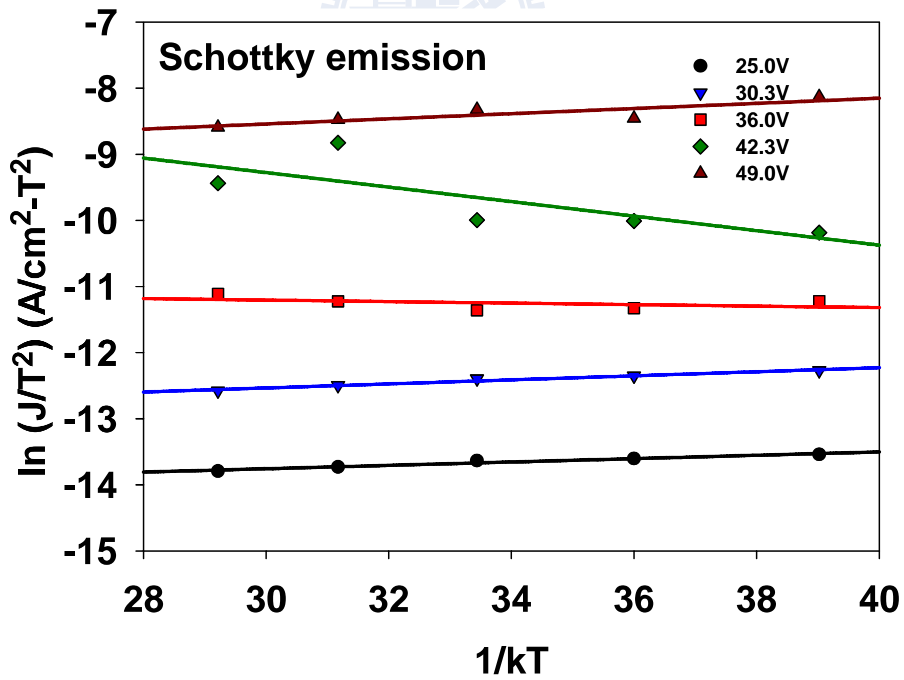

(b)

Figure 4.7 Schottky emission fitting

(a)*J-V* (b) the Schottky relationship of $\ln(J/T^2)$ verse 1/kT

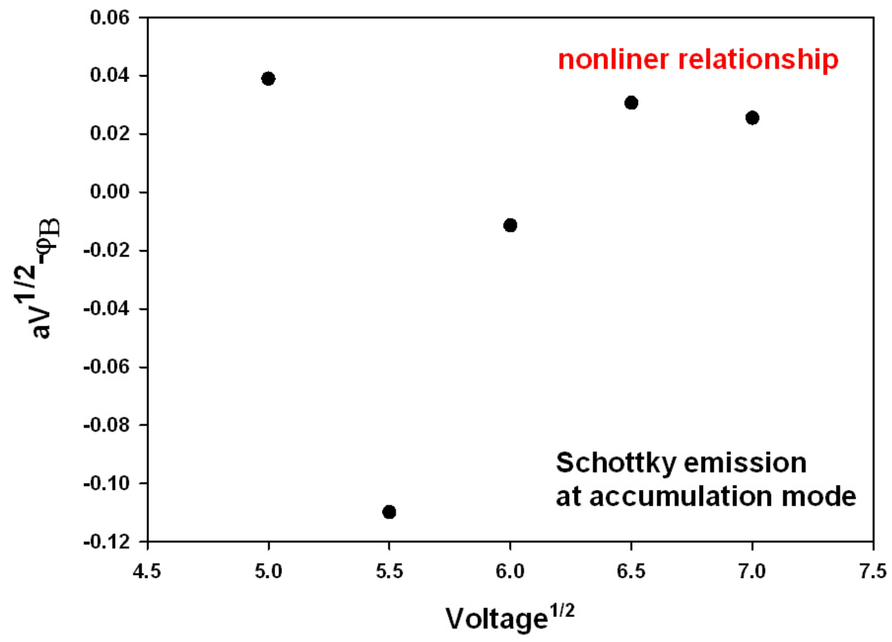

Figure 4.8 Extract slop from Fig.4.7(b)

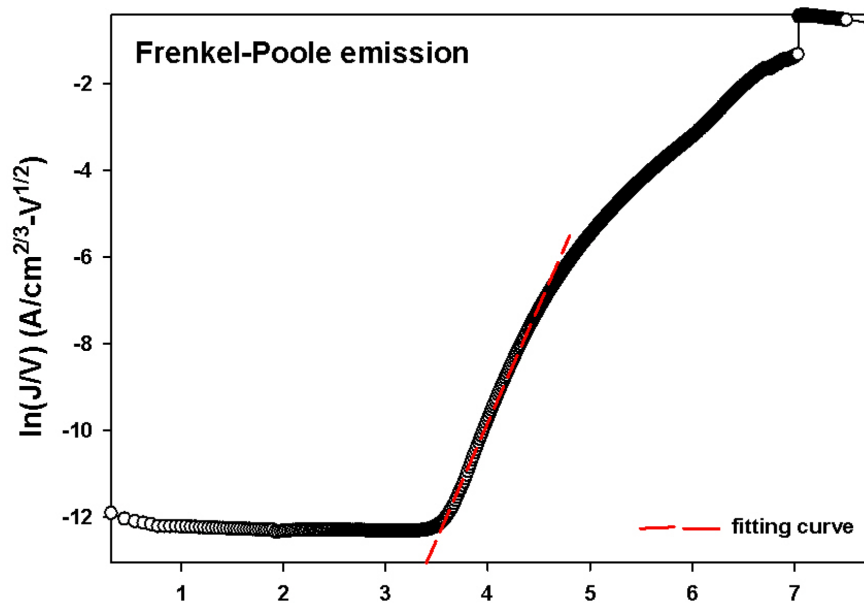

(a)

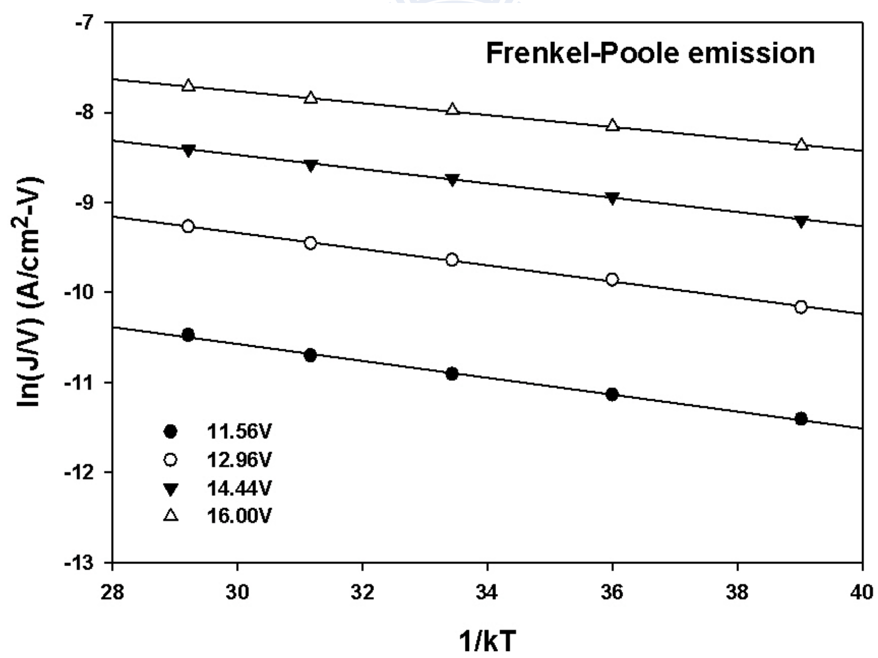

(b)

Figure 4.9 Frenkel-Poole emission fitting

(a)*J*-*V* (b) Frenkel-Poole thermal relationship

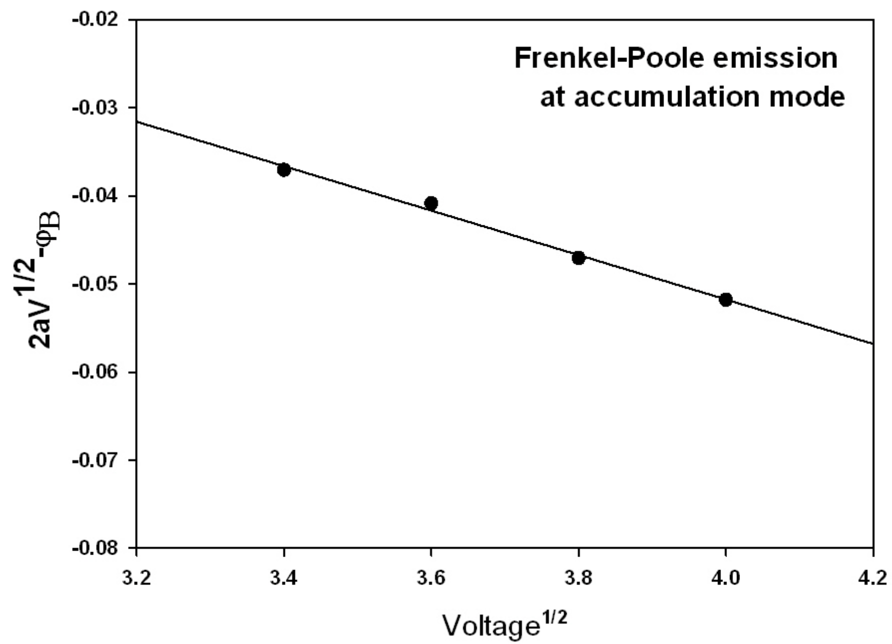

Figure 4.10 Extract slop from Fig.4.9(b)

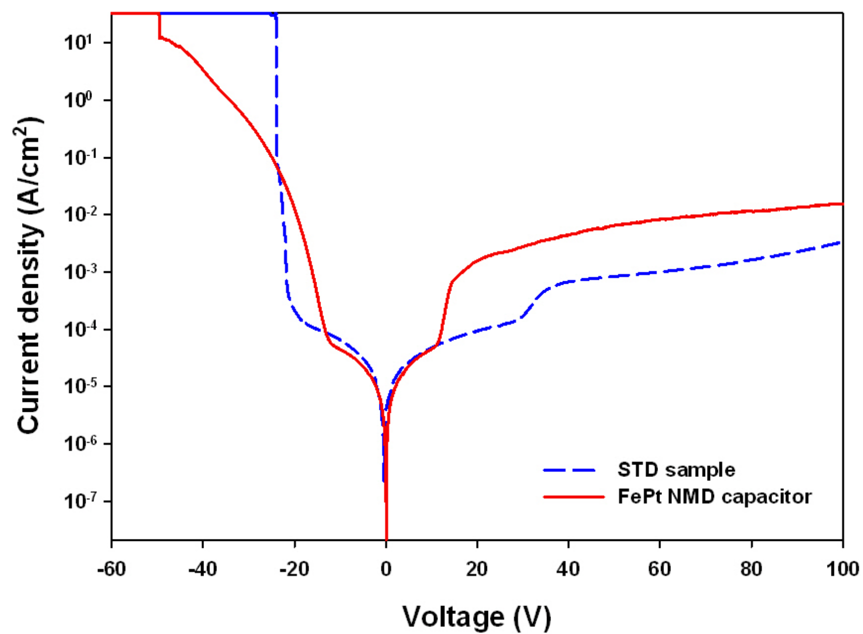

Figure 4.11, J-V characteristic of MIS capacitor compares with FePt MND and non-MND

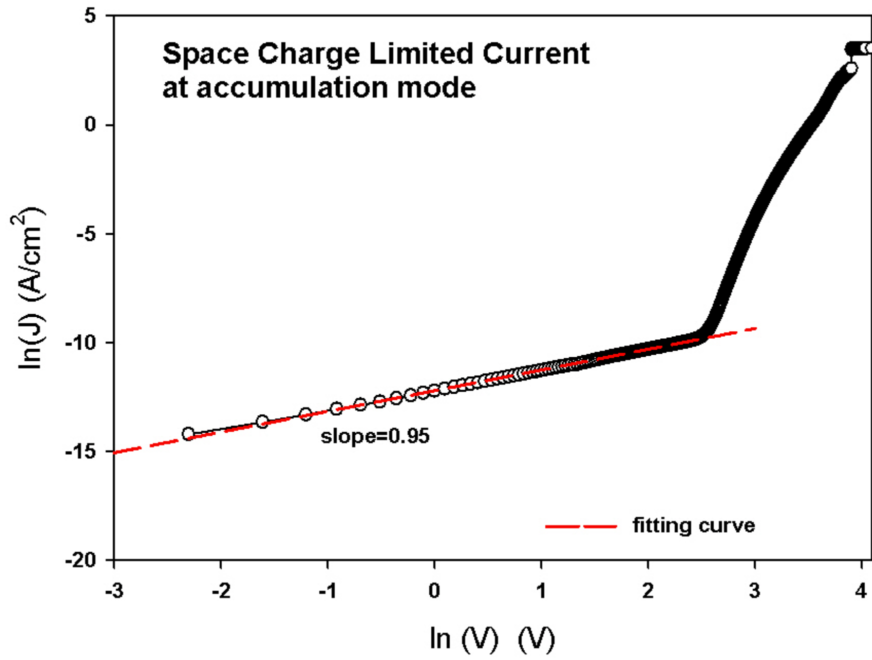

(a)

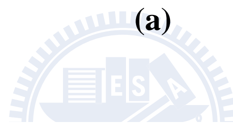

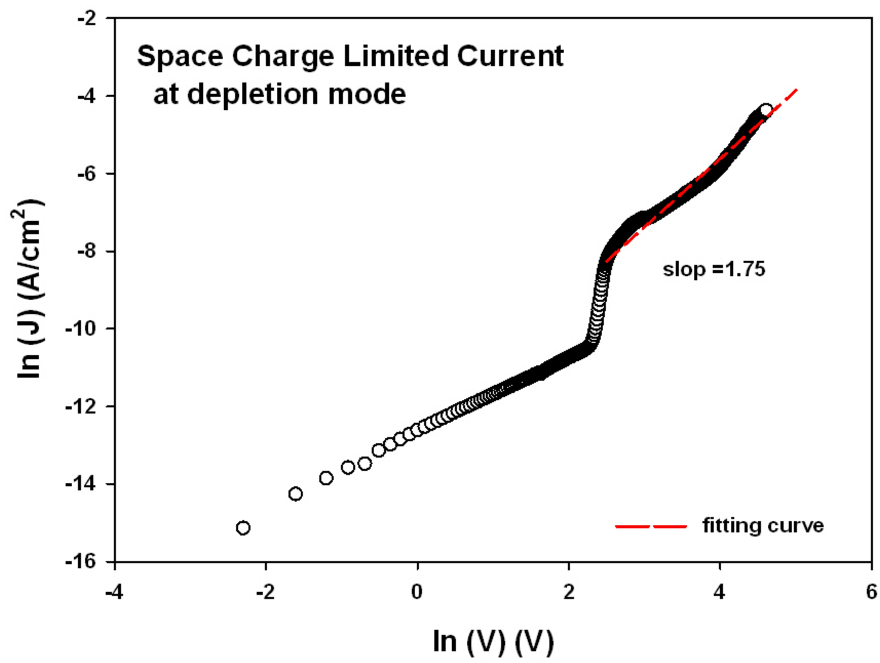

(b)

Figure 4.12 SCLC fitting (a)accumulation mode (b)depletion mode

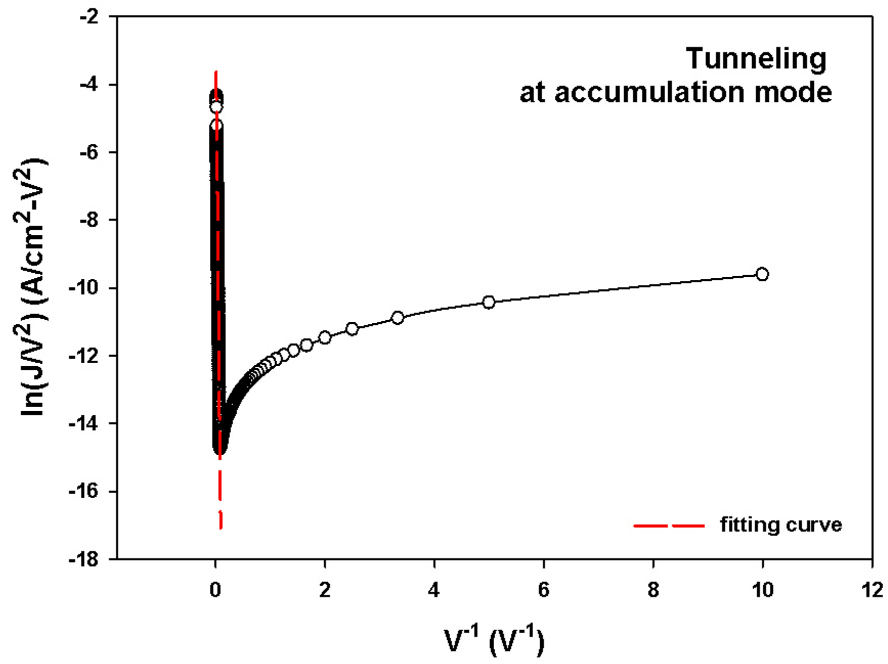

(a)

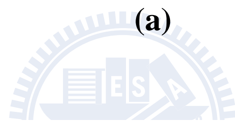

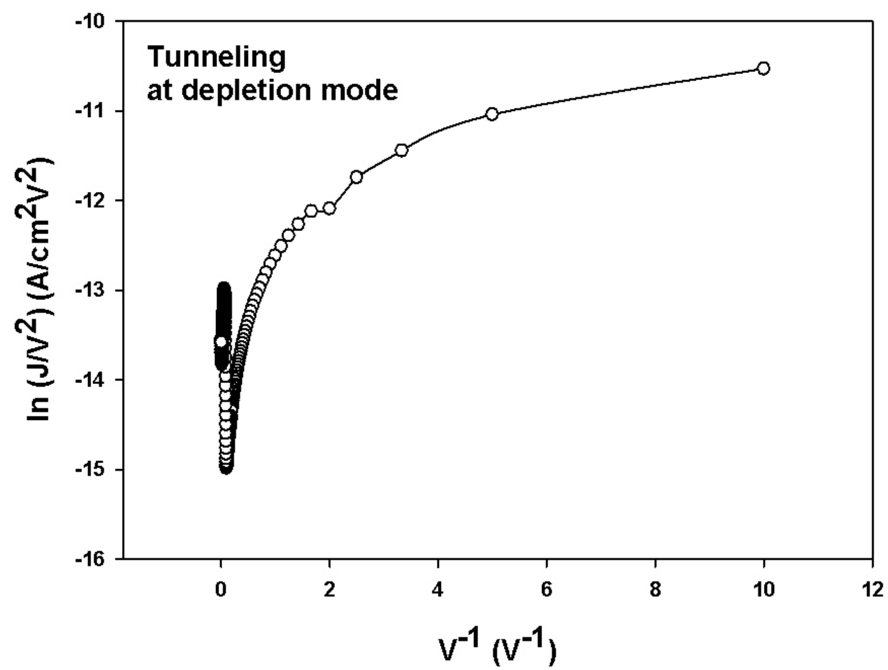

(b)

Figure 4.13Tunneling fitting (a)accumulation mode (b)depletion mode

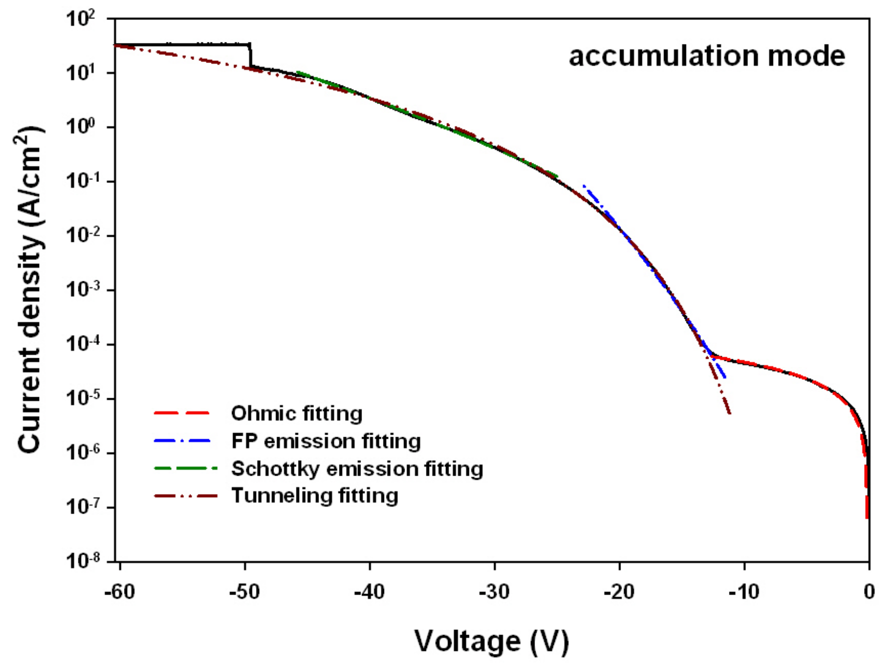

(a)

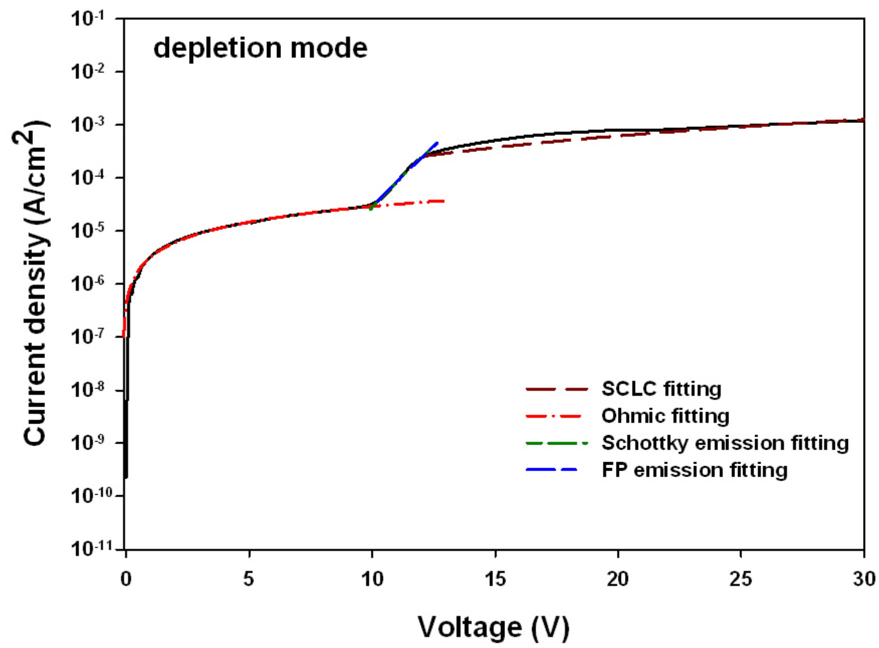

(b)

Figure 4.14 Leakage current mechanism fitting
(a) accumulation mode (b) depletion mode

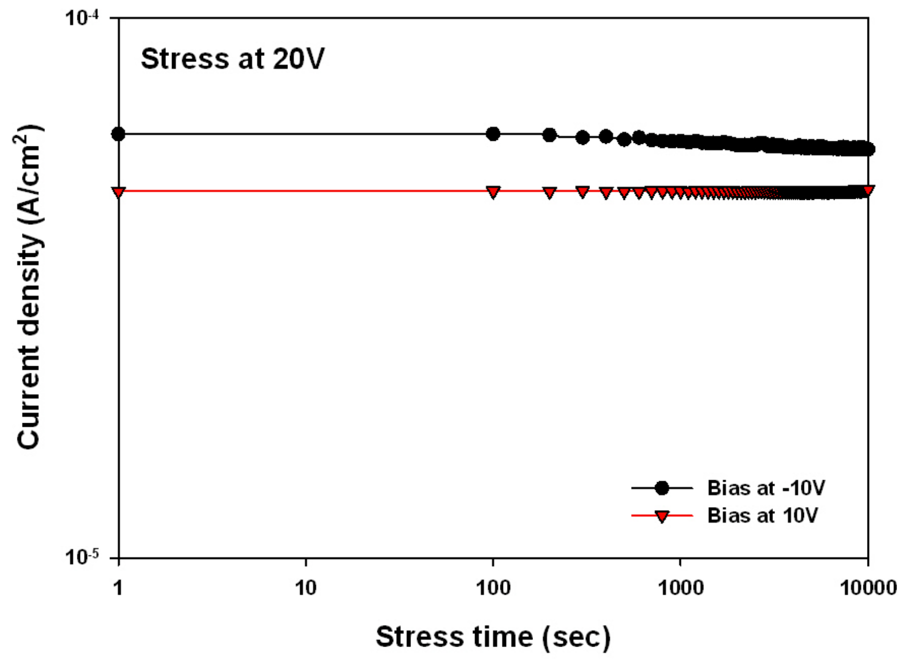

Figure 4.15 Current density with 20V constant voltage stress during 10000 second

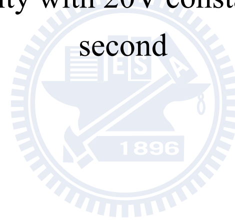

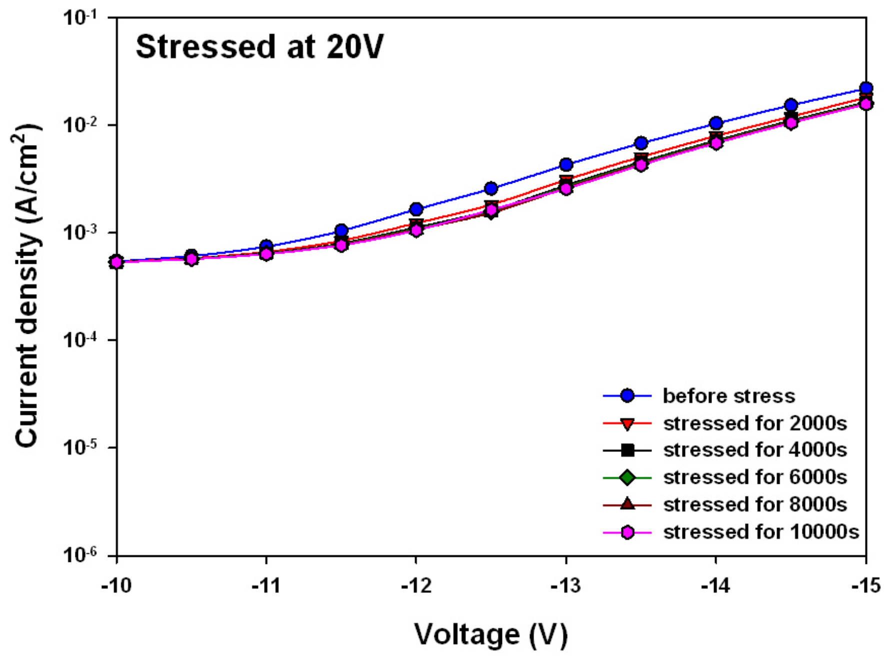

(a)

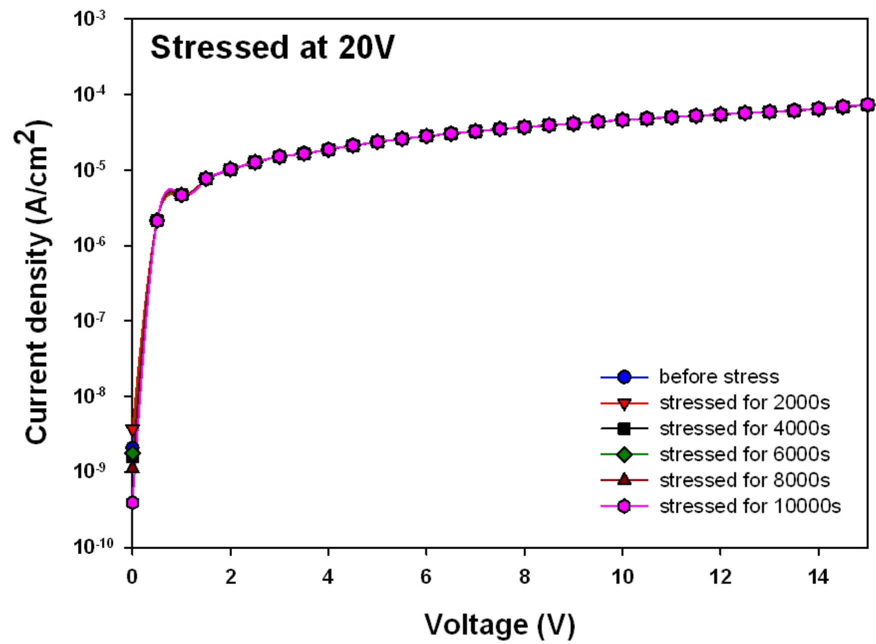

(b)

Figure 4.16 *J-V* with constant voltage stress (a)accumulation mode (b)depletion mode

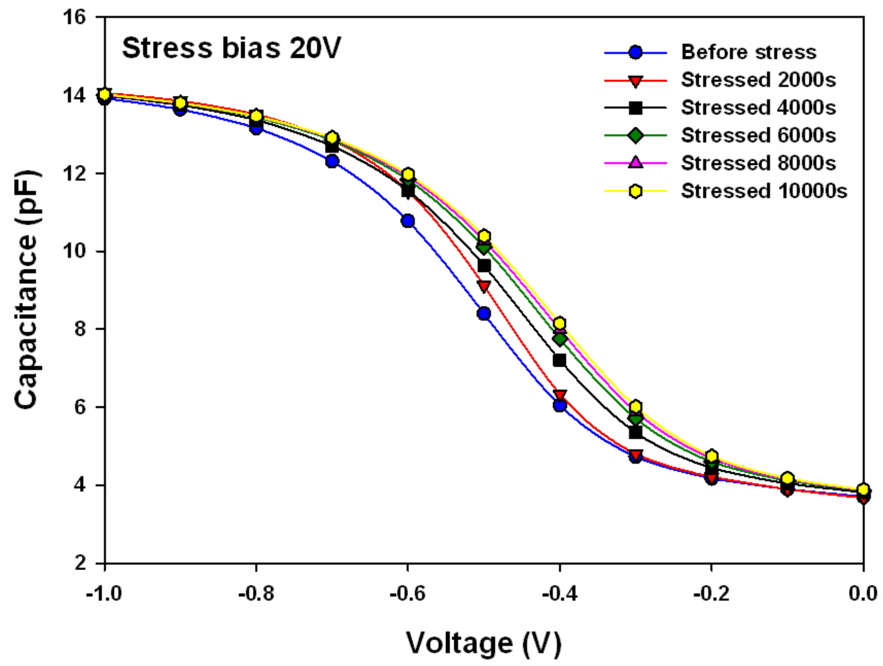

Figure 4.17 *C-V* with constant voltage stress 20V during 10000s

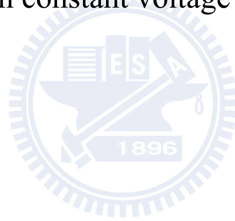

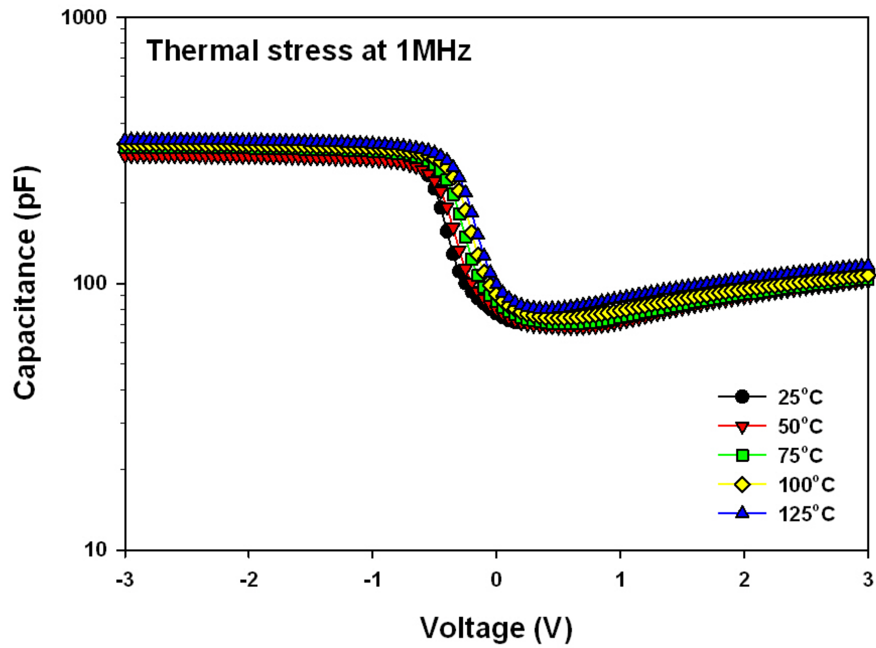

(a)

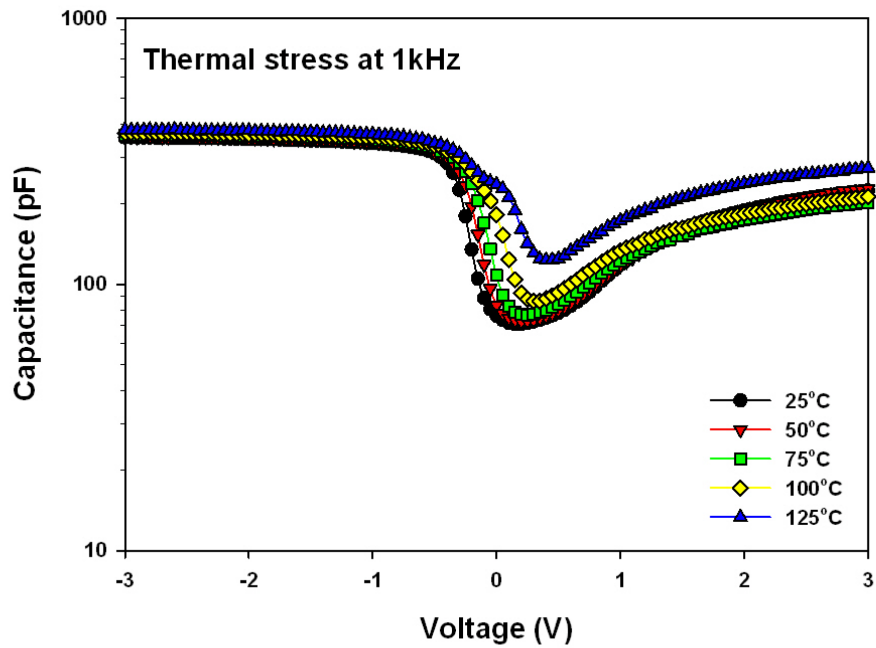

(b)

Figure 4.18 FePt MND capacitor *C-V* characteristic with thermal stress at (a)1MHz (b)1kHZ

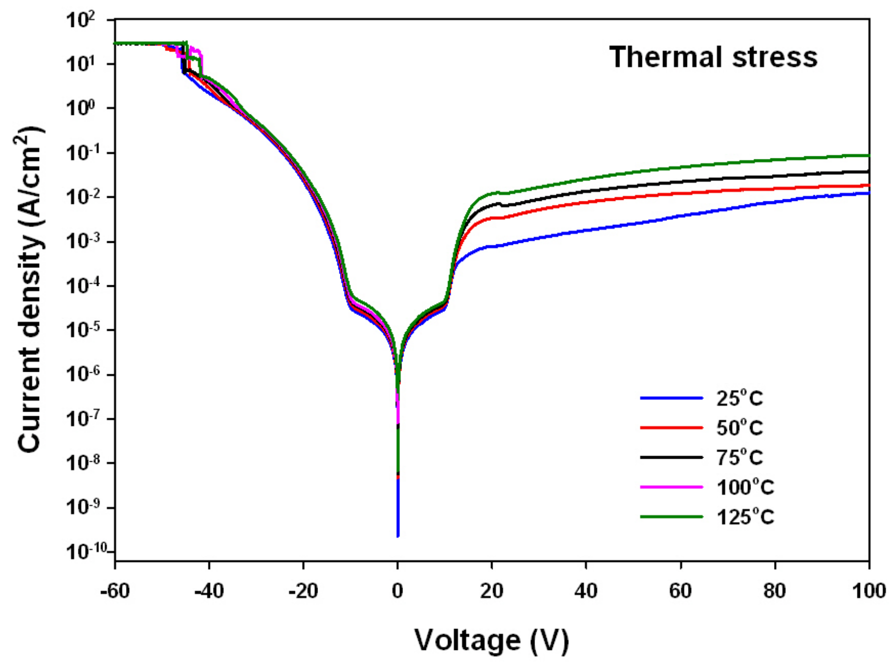

Figure 4.19 FePt MND capatior *J-V* characteristic with thermal stress

Chapter 5
Conclusion and Future Work

5.1 Conclusion

From quantum mechanics, magnetic field has a confinement effect that restricts the charge distribution and improves the insulating behavior. We take COMSOL as simulation tool to present this effect and fabricate FePt magnetic nanodots capacitors to proof this phenomenon.

The capacitor with magntic FePt nanodots has high breakdown electric strength; its leakage mechanism is different to general non-metal-dot capacitors. In accumulation mode, tunneling and Frenkel-Poole emission is the main mechanism because FePt nanodot is a possible trap provider. And magnetic field from FePt nanodots may make carrier tunnel though dielectric material difficultly that in result of high breakdown strength.

FePt nanodots existing in dielectric layer also enhance the static dielectric constant of silicon oxide. The electric polarizability is greatly increased because of the interface of FePt metal dots and silicon oxide and its magnetic properties. And under constant voltage stress +20V, the FePt MND capacitor has good characteristic in electric endurance.

5.2 Future Work

In future work, we can research the relationship of MND capacitor with different magnetic field strength and then progress to discuss the magnetic nanodots quantum confinement effect in different structure. Verify the role of parallel or vertical magnetic field in capacitor. Furthermore, this structural possibility for future flash memory [41], we can replace different material to study on its cell characteristics.

Reference

Charpter1

[1] *International Technology Roadmap of Semiconductors (ITRS)*, San Jose CA: SIA.

[2] T. Remmel, R. Ramprasad, and J.Walls, "Leakage behavior and reliability assessment of tantalum oxide dielectric MIM capacitors," in *Proc. Reliab Phys. Symp.*, 2003, pp. 277–281.

[3] H. Hu, C. X. Zhu, Y. F. Lu, M. F. Li, B. J. Cho, and W. K. Choi "A high performance MIM capacitor using HfO_2 dielectrics," *IEEE Electron Device Lett.*, vol. **23**, no. 9, pp. 514–516, Sep. 2002.

[4] Y. L. Tu, H. L. Lin, L. L. Chao, D. Wu, C. S. Tsai, C. Wang, C. F. Huang, C. H. Lin, and J. Sun, "Characterization and comparison of high-κ metal–insulator–metal (MIM) capacitors in 0.13 μm Cu BEOL for mixed-mode and RF applications," in *VLSI Symp. Tech. Dig.*, 2003, pp. 79–80.

[5] Y. K. Jeong, S. J. Won, D. J. Kwon, M. W. Song, W. H. Kim, O. H. Park, J. H. Jeong, H. S. Oh, H. K. Kang, and K. P. Suh, "High quality high-κ MIM capacitor by $Ta_2O_5/HfO_2/Ta_2O_5$ multilayered dielectric and NH_3 plasma interface treatments for mixed-signal/RF applications," in *VLSI Symp. Tech. Dig.*, 2004, pp. 222–223.

[6] H. Hu, S. J. Ding, H. F. Lim, C. X. Zhu, M. F. Li, S. J. Kim, X. F. Yu, J. H. Chen, Y. F. Yong, B. J. Cho, D. S. H. Chan, S. C. Rustagi, M. B. Yu, C. H. Tung, A. Y. Du, D. My, P. D. Foo, A. Chin, and D. L. Kwong, "High performance ALD $HfO_2-Al_2O_3$ laminate MIM capacitors for RF and mixed signal IC applications," in *IEDM Tech. Dig.*, 2003, pp. 15.6.1–15.6.4.

[7] Z. Liu, T. P. Chen,Y. Liu, M. Yang, J. I. Wong, and Z. H. Cen, "Static dielectric constant of Al nanocrystal/Al_2O_3 nanocomposite thin films determined by the capacitance-voltage reconstruction technique",in *Appl. Phys. Lett.* **96**, 173110 ,2010

[8] D. Weller, A. Moser, L. Folks, M. E. Best, W. Lee, M. F. Toney, M. Schwickert, J.-U. Thiele, and M. F. Doerner, *IEEE Trans. Magn.* **36**, 10~2000.

[9] B. M. Berkovsky, V. F. Medvedev, and M. S. Krakov, *Magnetic Fluids: Engineering Applications* ~Oxford University Press, Oxford, 1993.

[10] H. Zeng, J. Li, J. P. Liu, Z. L. Wang, and S. H. Sun, *Nature* ~London **420**,395 ~2002.

[11] M. Watanabe, T. Masumoto, D. H. Ping, and K. Hono, *Appl. Phys. Lett*. **76**, 3971 ~2000.

[12] A. Cebolleda, D. Weller, J. Sticht, G. R. Harp, R. F. C. Farrow, R. F. Marks, R. Savoy, and J. C. Scott, *Phys. Rev. B* **50**, 3419 ~1994.

[13] R. F. C. Farrow, D. Weller, R. F. Marks, M. F. Toney, A. Cebollada, and G. R. Harp, *J. Appl. Phys*. **79**, 5967 ~1996.

[14] S. H. Sun, C. B. Murray, D. Weller, L. Folks, and A. Moser, *Science* **287**, 1989 ~2000

[15] F. Fievet, J. P. Lagier, M. Figlarz, *MRS Bull.* **14**, 29 (1989).

[16] K. S. Suslick, M. Fang, T. Hyeon, *J. Am. Chem. Soc.* **118**, 11960 (1996).

[17] Cheng-Kuan YIN, Mariappan MURUGESAN1, Ji-Chel BEA, Mikihiko OOGANE, Takafumi FUKUSHIMA, Tetsu TANAKA, Shozo KONO, Seiji SAMUKAWA, and Mitsumasa KOYANAGI," New Magnetic Nanodot Memory with FePt Nanodots", *Japanese Journal of Applied Physics*, Vol. 46, No. 4B, 2007, pp. 2167–2171

Chapter 2

[18] Vladimir V. Mitin,Viatcheslav A. Kochelap, Michael A. Stroscio,*Quantum Heterostructures*, pp.73-75,Cambridge University Press,1999

[19] Vladimir V. Mitin,Viatcheslav A. Kochelap, Michael A. Stroscio,*Quantum Heterostructures*, pp.91-94,Cambridge University Press,1999

[20] Richard W. Robinett, *Quantum Mechanics-classical results, modern systems, and visualized examples,* pp.444-449, Oxford University Press,1997

[21] Patrik Fazekas, *Lecture Notes on Electron Correlation and Magnetism*, pp.19-28, World Scientific Publishing Co. Pte. Ltd. 1999

[22] Petra Denk, Martin Hartung,Martin Streibl, and Achim Wixforth ,Kenneth L. Campman and Arthur C.Gossard, "Magnetic-field-induced charge localization in a high-mobility semiconductor semiconductor superlattice", *Phys. Rev. B* **57**, number 20,1998

[23] Robert M. White, *Quantum Theory of Magnetism,*pp.200-204, McGRAW-HILL,1970

[24] Patrick A. Lee, Daniel S. Fisher, *Phys. Rev. Lett.* **47**, 882–885 (1981)

[25] D. V. Khveshchenko,"Magnetic-Field-Induced Insulating Behavior in Highly Oriented Pyrolitic Graphite", *Phys .Rev. Let* .**87**, 206401, 2001

Chapter 3

[26] Cheng-Kuan Yin, Mariappan Murugesan, Seiji Samukawa, Mitsumasa Koyanagi, "New Magnetic Nanodot Memory with FePt Nanodots ", *Jpn. J. Appl. Phys.*, vol.46, no.4B, 2007, pp.2167-2171.

Chapter 4

[27] M. H. Lu, T. Song, and T. J. Zhou et al. "FePt and Fe nanocomposite by annealing self-assembled FePt nanoparticles", *J. Appl. Phys.* **95**, no.11, part 2, 2004.

[28] An-Cheng Sun, P.C. Kuo, Jen-Hwa Hsu, H. L. Huang, Jui-Ming Sun, "Epitaxial growth mechanism of $L1_0$ FePt thin films on Pt/Cr bilayer with amorphous glass substrate"*J. Appl. Phys.* **98** 076109, 2005

[29] Toshio Suzuki and Kazuhiro Ouchi, *IEEE Transactions on Magnetics*, **37**, no.4, 2001

[30] S. M. Sze, Kwok K. Ng, *Physics of Semiconductor Devices*, John Wiley & Sons Inc, 2007, pp.227-236.

[31] Chih-sheng Kuo, Jui-feng Hsu et al. "High-k Al_2O_3 Gate Dielectrics", *IEEE Transactions on electron devices*, vol. 51,no. 6, 2004

[32] Takio Hikono, Takashi Matsumura, Atsushi Miura, Yukiharu Uraoka et al. "Electron confinement in a metal nanodot monolayer embedded in silicon dioxide produced using ferritin protein", *Appl. Phys. Lett.* **88**, 023108, 2006

[33] M. Gauthie, *Engineered Materials Handbook Desk Edition*, the materials information society, 1995.

[34] R. Dupree, M. A. Smithard, "The electronic properties of small metal particles: the electric polarizability", *J. Phys. C*, vol.5, 1972.

[35] S. Strässler and M. J. Rice, P. Wyder, "Comment on Gorkov and Elishberg's Result for the Polarizability of a Minute Metallic Particle",*Phys. Rev. B*, vol 6, no.7,1972

[36] Vishal Singh, A. R. Kulkarni, T. R. Rama Mohan,"Dielectric Properties of Aluminum-Epoxy Composites", *Jou. of Appl. Poly. Sci.*, vol. 90, 3602-3608, 2003

[37] Z. Liu, T. P. Chen, Y. Liu, M. Yang et al, "Static dielectric constant of Al nanocrystal/Al_2O_3 nanocomposite thin films determined by the capacitance-voltage reconstruction technique", *Appl. Phys. Lett.* **96**, 173110, 2010

[38] R. Bartnikas, "Performance characteristicd of dielectricd in the presence of space charge", *IEEE Transactions on Dielectrics and Electrical Insulation*, vol.4, no.5, 1997

[39] Chi-Chao Hung, Anthony S. Oates, Horng-Chih Lin, Yu-En Percy Chang, Jia-Lian Wang, Cheng-Chung Huang and You-Wen Yau, "An innovative

Understanding of Metal-Insulator-Metal (MIM)-Capacitor Degradation Under Constant-Current Stress," *IEEE Trans. Electron Devices*, vol. 7, no. 3, pp. 462-467, Sep. 2007.

[40] S. M. Sze, Kwok K. Ng, *Physics of Semiconductor Devices*, John Wiley & Sons Inc, 2007, pp.40-45.

Chapter 5

[41] Ji chel Bea, Yun Heub Song, Kang-Wook Lee, Gae-Hun Lee, Tetsu Tanaka and Mitsumasa Koyanagi, "Cell characteristics of a mltiple alloy nano-dots memory structure"*Semicond. Sci. Technol.* **24**,2009,085013